

London penetration depth in iron base superconductors*

18

I. Introduction

During the years between this publication and the second edition (published in 2007), a new family of superconductors has been discovered and widely studied, namely an iron-based variety. After the first reports of superconductivity in LaFePO with $T_c \approx 4$ K (Kamihara et al., 2006) and then in LaFeAs(OF) with $T_c \approx 26$ K (Kamihara et al., 2008), a transition temperature T_c as high as 55 K was eventually reported in SmFeAs($O_{1-x}F_x$) (Ren et al., 2008). These findings triggered an extensive research effort seeking to understand the fundamental physics underlying superconductivity in this new family. Subsequent to the original reports, at least seven different classes of Fe-based superconductors have been identified, all exhibiting unconventional physical properties (Johnston, 2010; Mazin, 2010; Paglione and Greene, 2010; Stewart, 2011). Among those, perhaps the most diverse family is based on (AE)FeAs parent compounds (where AE signifies alkaline earth, denoted the “122” system) in which electron (Sefat et al., 2008; Ni et al., 2010a, b; Canfield and Bud’ko, 2010), hole (Rotter et al., 2008; Ni et al., 2008a, b), and iso-
valent (Ren et al., 2009; Jiang et al., 2009) dopants induce a superconductivity “dome” with a maximum T_c achieved at fairly high dopant concentrations (up to 45% in the case of BaK122). In addition, superconductivity and long-range magnetic order coexist for under-doping.

After more than 3 years into the intense study of these Fe-based superconductors, several experimental conclusions supported by a large number of reports can be adduced. Among those, relevant to our treatment of the London penetration depth, are (1) two distinct superconducting gaps with a magnitude ratio of about 2; (2) power-law behavior of thermodynamic quantities at low temperature presumably due to pair-breaking scattering and gap anisotropy; (3) doping dependent three-dimensional gap structures with possible nodes. For some reviews of various experiments and theories, refer to the following references: Johnston (2010), Mazin (2010), Paglione and Greene (2010), Stewart (2011), Canfield and Bud’ko (2010), Mizuguchi and Takano (2010), Wilson (2010), Maiti et al. (2011), and Hosono (2008). In this chapter, we focus on the London penetration depth λ as a sensitive tool to study superconducting gap structure, albeit averaged over the Fermi surface (Prozorov and Giannetta, 2006).

*This section is based on the original research paper by R. Prozorov and V. G. Kogan, “London penetration depth in iron-based superconductors”, Rep. Prog. Phys. 74, 124505 (2011).

A. Measurements of the London penetration depth

There are several ways to measure magnetic penetration depths λ in superconductors (Prozorov and Giannetta, 2006). These include muon-spin rotation (μ SR) (Luetkens et al., 2008; Williams et al., 2010; Sonier et al., 2011), frequency-dependent conductivity (Valdés Aguilar et al., 2010; Wu et al., 2010), magnetic force and superconducting quantum interference device (SQUID) microscopy (Luan et al., 2010, 2011), determinations of the first critical field using either global (Prozorov et al., 2009a; Song et al., 2011) or local probes (Okazaki et al., 2009; Klein et al., 2010), microwave cavity perturbation (Hashimoto et al., 2009a, b; Shibauchi et al., 2009; Bobowski et al., 2010; Takahash et al., 2011), mutual inductance (particularly suitable for thin films; Yong et al., 2011), and self-oscillating tunnel-diode resonator (TDR; Prozorov et al., 2009a; Shibauchi et al., 2009; Malone et al., 2009; Gordon et al., 2010; Kim et al., 2011a,b; Martin et al., 2009a, b, 2010a, b).

Each technique has its advantages and disadvantages and only by a combination of several different measurements performed on different samples and under different experimental conditions can we obtain a more or less objective picture. In the case of Fe-based superconductors, most of the reports agree in general, but yet differ in details. Most difficulties arise from the need to resolve very small variations of the penetration depth at the lowest temperatures (below 1 K) while maintaining extreme temperature resolution and the ability to measure statistically a sufficient number of data points over the entire temperature range. In addition, it is important to look at a general picture by measuring many samples of each composition and over an extended doping regime. This review is based on the results obtained with a self-oscillating TDR that has the advantage of providing stable resolution of about 1 part per 10^9 (Prozorov and Giannetta, 2006). Indeed, a comparison of TDR with other techniques, especially bulk probes, such as thermal conductivity, is important for reaching a consensus regarding the gap structure in pnictide superconductors (Luo et al., 2009; Tanatar et al., 2010; Reid et al., 2010).

II. TDR measurements

A. Frequency-domain measurements

When a nonmagnetic conducting sample is inserted into the coil of a tank circuit of quality factor Q and resonance frequency $f_0 = 1/2\pi\sqrt{L_0C}$, it induces changes in this frequency and the quality factor. For a flat slab of width 2ω and volume V_s in a parallel field (Hardy et al., 1993):

$$\frac{\Delta f}{f_0} = \frac{f_0 - f(\alpha)}{f_0} = \frac{V_s}{2V_c} \left(1 - \Re \frac{\tanh(\alpha\omega)}{\alpha\omega} \right) \quad (18.1)$$

$$\frac{\Delta f}{f_0} = \frac{f_0 - f(\alpha)}{f_0} = \frac{V_s}{2V_c} \left(1 - \Re \frac{\tanh(\alpha\omega)}{\alpha\omega} \right), \quad (18.2)$$

where $\alpha = (1 - i)/\delta$ in a normal metal and $\alpha = 1/\lambda$ in a superconductor. Here, δ is the normal skin depth and λ is the London penetration depth. V_c is the volume of the inductor. Solving explicitly, we have for a normal metal:

$$\frac{\Delta f}{f} = \frac{V_s}{2V_c} \left(1 - \frac{\delta}{2\omega} \frac{\sinh \frac{2\omega}{\delta} + \sin \frac{2\omega}{\delta}}{\cosh \frac{2\omega}{\delta} + \cos \frac{2\omega}{\delta}} \right) \quad (18.3)$$

and, in a superconductor, we obtain the known “infinite slab” solution:

$$\frac{\Delta f}{f} = \frac{V_s}{2V_c} \left(1 - \frac{\lambda}{\omega} \tanh \left(\frac{\omega}{\lambda} \right) \right), \quad (18.4)$$

which allows us to measure both the superconducting penetration depth, and the normal state skin depth (which provides the contactless measure of resistivity).

In the case of a finite sample with magnetic susceptibility χ , we can still write $\Delta f = -4\pi\chi(T)G$, where $G \approx \frac{f_0 V_s}{2V_c(1-N)}$ is a geometric calibration constant that includes the effective demagnetization factor N (Prozorov et al., 2000a). The constant G is measured directly by pulling the sample out of the coil (Prozorov and Giannetta, 2006; Prozorov et al., 2000a). The susceptibility in the Meissner state can be written in terms of the London penetration depth $\lambda(T)$ and the normal state paramagnetic permeability (if local-moment magnetic impurities are present), $\mu(T)$, as (Prozorov et al., 2000a):

$$4\pi\chi = \frac{\sqrt{\mu(T)\lambda(T)}}{R} \tanh \left(\frac{\sqrt{\mu(T)R}}{\lambda(T)} \right) - 1, \quad (18.5)$$

where R is the characteristic sample dimension. For a typical experiment slab geometry with $2b \geq 2a$ planar dimensions and thickness $2d$ (magnetic field excitation is along the d -side), R is approximately given by (Prozorov et al., 2000a):

$$\frac{\omega}{R} \approx 2 \left[1 + \left(1 + \left(\frac{2d}{\omega} \right)^2 \right) \tan^{-1} \left(\frac{\omega}{2d} \right) - \frac{2d}{\omega} \right] \quad (18.6)$$

with $\omega \approx ab/(a+b)$.

Unlike the microwave cavity perturbation technique that requires scanning the frequency (Hardy et al., 1993), TDR is a self-oscillating resonator always locked onto its resonant frequency (Van Degrift, 1975). A sample to be studied is mounted on a sapphire rod and inserted into the inductor coil of the tank circuit. Throughout the measurement the temperature of the circuit (and of the coil) is stabilized at ± 1 mK. This is essential for the stability in the resonant frequency, which is resolved to about 0.01 Hz. This translates to the ability to detect changes in $\lambda(T)$ in

the range of a few angstroms. The ac magnetic excitation field, H_{ac} , in the coil is about 20 mOe, which is small enough to ensure that no vortices are created and London penetration depth is measured.

B. Measurements of the absolute value of $\lambda(T)$

The previously described TDR technique provides precise measurements of the *variation* of the penetration depth, $\Delta\lambda(T)$, but not its absolute value for the reasons described in detail elsewhere (Prozorov et al., 2000b). However, the TDR technique can be extended to obtain the absolute value of the penetration depth, $\lambda(T)$. The idea is to coat the entire surface of the superconductor under study with a thin film of a conventional superconductor with lower T_c and a known value of $\lambda(0)$. In this work we used aluminum, which is convenient, since its $T_c^{\text{Al}} \approx 1.2$ K is quite low for most of the discussed materials, so it is possible to extrapolate to $T=0$ and obtain $\lambda(0)$. While the Al film is superconducting it screens the magnetic field and the effective penetration depth is (Gordon et al., 2010):

$$\lambda_{\text{eff}}(T) = \frac{\lambda_{\text{Al}}(T) \left(\lambda(T) + \lambda_{\text{Al}}(T) \tanh\left(\frac{t}{\lambda_{\text{Al}}(T)}\right) \right)}{\lambda_{\text{Al}}(T) + \lambda(T) \tanh\left(\frac{t}{\lambda_{\text{Al}}(T)}\right)}, \quad (18.7)$$

However, when it becomes normal, the Al layer does not produce any screening because its thickness, t , is much less than the normal state skin depth at the TDR operating frequency of 14 MHz, where $\delta_{\text{Al}} \approx 75 \mu\text{m}$ for $\rho_0^{\text{Al}} = 10 \mu\Omega\cdot\text{cm}$ (Hauser, 1972). By measuring the frequency shift upon warming from the base temperature, $T = T_{\min}$ to $T = T_c^{\text{Al}}$, where $\lambda_{\text{Al}} \rightarrow \infty$ and Eq. (18.7) gives $\lambda_{\text{eff}}(T_c^{\text{Al}}) = t + \lambda(T_c^{\text{Al}})$, we can calculate $\lambda(T_c^{\text{Al}})$. We also note that if the aluminum coating is damaged (i.e., by cracks and/or holes), the result will *underestimate* $\lambda(0)$. This method, therefore, provides the lower boundary estimate.

C. Out-of-plane penetration depth

Finally, the TDR technique can be used to measure the out-of-plane component of the penetration depth, λ_c . For the excitation field $H_{\text{ac}}||c$, screening currents flow only in the a , b -plane and Δf is only related to the in-plane penetration depth, $\Delta\lambda_{ab}$. However, when the magnetic field is applied along the a , b -plane ($H_{\text{ac}}||ab$), screening currents flow both in the plane and between the planes, along the c -axis. In this case, Δf^\perp contains contributions from both $\Delta\lambda_{ab}$ and $\Delta\lambda_c$. For a rectangular sample of thicknesses $2t$, width 2ω , and length l , Δf^\perp is approximately given by Eq. (18.8):

$$\frac{\Delta f^\perp}{\Delta f_0^\perp} \approx \frac{\Delta\lambda_{ab}}{t} + \frac{\Delta\lambda_c}{\omega} = \frac{\Delta\lambda_{\min}}{R_b}, \quad (18.8)$$

where R_b is the effective dimension that takes into account finite size effects (Prozorov et al., 2000a; Eq. (18.6)). Knowing $\Delta\lambda_{ab}$ from the measurements with $B_1ac \parallel c$ and the sample dimensions, we can obtain $\Delta\lambda_c$ from Eq. (18.8). However, because $2\omega \geq 4 \times 2t$ in most cases, Δf^\perp is in general dominated by the contribution from $\Delta\lambda_{ab}$. The subtraction of $\Delta\lambda_c$ therefore becomes prone to large errors. The alternative, more accurate approach is to measure the sample twice (Fletcher et al., 2007). After the first measurement with the field along the longest side l , ($B_1ac \parallel l$), the sample is cut along this l direction into two halves, so that the width (originally 2ω) is reduced to ω . Since the thickness $2t$ remains the same, we can now use Eq. (18.8) to calculate $\Delta\lambda_c$ without knowing $\Delta\lambda_{ab}$. Note that the length l and width ω are in the crystallographic a , b -plane, whereas the thickness $2t$ is measured along the c -axis. In our experiments, both approaches to estimate $\Delta\lambda_c(T)$ produced a similar temperature dependence, but the former technique had a larger data scatter, as expected.

III. London penetration depth and superconducting gap

In order to describe London penetration depth in multigap superconductors and to take into account pair-breaking scattering, we use the weak-coupling Eilenberger quasiclassical formulation of superconductivity theory that holds for a general anisotropic Fermi surface and for any gap symmetry (Eilenberger, 1968). This method, suitable for the analysis of the experimental data, is described in a few publications of one of us (Gordon et al., 2009a, b; Kogan, 2002, 2009; Kogan et al., 2009); here we briefly summarize the scheme.

In the clean case the Eilenberger equations read:

$$v \prod f = \frac{2\Delta g}{\hbar} - 2\omega f, \quad (18.9)$$

$$-v \prod^- f^+ = \frac{2\Delta^* g}{\hbar} - 2\omega f^+, \quad (18.10)$$

$$g^2 = 1 - ff^+, \quad (18.11)$$

$$\Delta(r, v) = 2\pi TN(0) \sum_{\omega > 0}^{\omega D} \langle V(v, v') f(v', r, \omega) \rangle'_v, \quad (18.12)$$

$$j = -4\pi|e|N(0)Tl_m \sum_{\omega > 0} \langle vg \rangle. \quad (18.13)$$

Here, v is the Fermi velocity, $\Pi = \nabla + 2\pi iA/\phi_0$; ϕ_0 is the flux quantum; and $\Delta(r)$ is the gap function (the order parameter), which may depend on the position k_F at the Fermi surface (or on v). Eilenberger functions $f(r, v, \omega)$, f^+ and g originate

from Gor'kov Green's functions integrated over the energy variable near the Fermi surface to exclude fast spatial oscillations on the scale $1/k_F$; instead f, g vary on the relevant superconductivity scale comparable to the coherence length ξ . The functions f, f^+ describe the superconducting condensate, whereas g represents normal excitations. $N(0)$ is the total density of states at the Fermi level per spin. The Matsubara frequencies are defined by $\hbar\omega = \pi T(2n + 1)$ with integer n , and ω_D being the Debye frequency for phonon-mediated superconductivity or a relevant energy scale for other mechanisms. The averages over the Fermi surface weighted with the local density of states $\propto 1/|v|$ are defined as

$$\langle X \rangle = \int \frac{d^2 k_F}{(2\pi)^3 \hbar N(0) |v|} X. \quad (18.14)$$

The order parameter Δ is related to f in the self-consistency equation Eq. (18.12). Often, the effective coupling V is assumed to be factorizable (Markowitz and Kadanoff, 1963), $V(v, v') = V_0 \Omega(v) \Omega(v')$; this assumption is not always justifiable, but it makes the algebra much simpler. We look for the order parameter in the form $\Delta(\mathbf{r}, T; \mathbf{v}) = \psi(\mathbf{r}, T) \Omega(\mathbf{v})$. Then, the self-consistency Eq. (18.12) takes the form:

$$\psi(r, T) = 2\pi T N(0) V_0 \sum_{\omega > 0}^{\omega_D} \langle \Omega(v) f(v, r, \omega) \rangle. \quad (18.15)$$

The function $\Omega(\mathbf{v})$ (or $\Omega(\mathbf{k}_F)$), which describes the variation along the Fermi surface, is conveniently normalized (Pokrovskii, 1961):

$$\langle \Omega^2 \rangle = 1. \quad (18.16)$$

In the absence of currents and fields $\Pi = 0$, and the Eilenberger equations give for the uniform ground state:

$$f_0 = f_0^+ = \frac{\Delta_0}{\beta}, \quad g_0 = \frac{\hbar\omega}{\beta}, \quad \beta^2 = \Delta_0^2 + \hbar^2 \omega^2; \quad (18.17)$$

Note that in general, both $\Delta_0 = \psi_0(T) \Omega(\mathbf{k}_F)$ and β depend on the position at the Fermi surface.

Instead of dealing with the effective microscopic electron-electron interaction V , we can use in this formal scheme the measurable critical temperature T_c by utilizing the identity

$$\frac{1}{N(0)V_0} = \ln \frac{T}{T_c} + 2\pi T \sum_{\omega > 0}^{\omega_D} \frac{1}{\hbar\omega'} \quad (18.18)$$

which is equivalent to the famous relation $\Delta(0) = \pi T_c e^{-\gamma} = 2\hbar\omega_D \exp(-1/N(0)V_0)$; $\gamma = 0.577$ is the Euler constant. Substituting Eq. (18.18) in Eq. (18.5) and replacing ω_D with infinity due to fast convergence:

$$\frac{\psi}{2\pi T} \ln \frac{T_c}{T} = \sum_{\omega>0}^{\infty} \left(\frac{\psi}{\hbar\omega} - \langle \Omega f \rangle \right). \quad (18.19)$$

Now the equation for $\psi(T)$ reads:

$$\frac{1}{2\pi T} \ln \frac{T_c}{T} = \sum_{\omega>0}^{\infty} \frac{1}{\hbar\omega} - \left(\frac{\Omega^2}{\sqrt{\psi^2\Omega^2 + \hbar^2\omega^2}} \right). \quad (18.20)$$

A. London penetration depth

Within microscopic theory, the penetration of weak magnetic fields into superconductors is treated perturbatively. Weak super currents and fields leave the order parameter modulus unchanged, but cause the condensate (i.e., Δ) and the amplitudes f to acquire an overall phase $\theta(r)$. Using the method of perturbations, we obtain corrections to f_0 , g_0 among which we need only

$$g_1 = i\hbar \frac{\Delta_0^2}{2\beta^3} v \left(\nabla\theta + \frac{2\pi A}{\phi_0} \right). \quad (18.21)$$

Substituting this in the general expression, Eq. (18.13), for the current density, we obtain the London relation between the current and the “gauge invariant vector potential” $\alpha = \phi_0 \nabla\theta/2\pi + A$:

$$\frac{4\pi j_i}{c} = -(\lambda^2)_{ik}^{-1} a_k. \quad (18.22)$$

Then, the general expression (18.13) for the current gives the inverse tensor of the squared penetration depth:

$$(\lambda^2)_{ik}^{-1} = \frac{16\pi^2 e^2 T}{c^2} N(0) \sum_w \left\langle \frac{\Delta_0^2 v_i v_k}{\beta^3} \right\rangle \quad (18.23)$$

This result holds at any temperature for clean materials with an arbitrary Fermi surface and order parameter anisotropies (Kogan, 2002). The temperature dependence of $\Delta_0 = \psi\Omega$ and β can be obtained by solving Eq. (18.20).

Thus, the general approach for the evaluation of $\lambda(T)$ in clean superconductors consists of two major steps: first evaluate the order parameter $\Delta_0(T)$ in the uniform zero-field state for a given gap anisotropy $\Omega(v)$, then use Eq. (18.23) with a proper

averaging over the Fermi surface. The sum over Matsubara frequencies is rapidly convergent and is easily done numerically (except in a few limiting situations for which analytic evaluation is possible).

B. Isotropy on a general Fermi surface

For the majority of materials with an electron–phonon interaction responsible for superconductivity, the relevant phonons have frequencies on the order of ω_D . We can see that in exchanging such phonons, the electron momentum transfer is of the order of $\hbar k_F$; this leads to considerable smoothing of (k_F) (Abrikosov, 1988). Indeed, in such materials (k_F) is nearly constant along the Fermi surface, the strong possible anisotropy of the latter notwithstanding. In this case, commonly called “*s*-wave,” Δ is taken as constant at the Fermi surface:

$$(\lambda^2)_{ik}^{-1} = \frac{8\pi^2 e^2 N(0) \langle v_i v_K \rangle}{c^2} 2\pi T \Delta^2 \sum_w \frac{1}{\beta^3}. \quad (18.24)$$

We obtain in the Ginzburg–Landau domain:

$$(\lambda^{-2})_{ik}^{(-1)}(T \rightarrow T_c) = 2(\lambda^{-2})_{ik}^{(-1)}(0)(1-t), \quad t = T/T_c. \quad (18.25)$$

At low temperatures:

$$\frac{\Delta(T)}{T_c} = \frac{\Delta(0)}{T_c} - \sqrt{\frac{2\pi T \Delta(0)}{T_c^2}} e^{-\frac{\Delta(0)}{T}} \approx 1.764 - 3.329 \sqrt{t} e^{-\frac{1.764}{t}}. \quad (18.26)$$

The low-temperature behavior of the penetration depth is given by:

$$(\lambda^2)_{ik}^{-1} = (\lambda^2)_{ik}^{-1}(0) \left(1 - 2 \sqrt{\frac{\pi \Delta(0)}{T}} e^{-\frac{\Delta(0)}{T}} \right). \quad (18.27)$$

C. 2D d-wave

As an example of an anisotropic Δ , let us take a relatively simple but important case of a *d*-wave order parameter on the two-dimensional cylindrical Fermi surface: $\Omega = \Omega_0 \cos 2\varphi$, where φ is the properly chosen azimuth angle on the Fermi cylinder. With this choice, the gap node s is at $\varphi = \pm \pi/4, \pm 3\pi/4$. The normalization Eq. (18.16) gives $\Omega_0 = \sqrt{2}$, so that $\Delta_0 = \sqrt{2} \cos 2$. The order parameter at $T = 0$ is now given by:

$$\frac{\Delta_{\max(T)}}{T_c} \approx \frac{2\pi}{e^{\gamma+0.5}} \approx 2.139. \quad (18.28)$$

and at $T \ll T_c$:

$$\frac{\Delta_{\max(T)}}{T_c} \approx 2.139 - 0.927t^3. \quad (18.29)$$

After averaging over the Fermi cylinder we obtain for the in-plane penetration depth:

$$\lambda^{-2}(T) = \lambda^{-2}(0) \left(1 - \sqrt{2} \frac{T}{\Delta_m} \right), \quad (18.30)$$

$$\lambda^{-2}(0) = \frac{4\pi e^2 N(0)v^2}{c^2}. \quad (18.31)$$

D. Eilenberger two-gap scheme: the weak-coupling model

The full-blown microscopic approach based on the Eliashberg theory is quite involved and not easy for the data analysis (Golubov and Mazin, 1997; Brinkman et al., 2002; Dolgov et al., 2005; Nicol and Carbotte, 2005); hence the need for a relatively simple but justifiable, self-consistent, and effective scheme that experimentalists can employ. The weak-coupling model is such a scheme. Over the years, the weak-coupling theory had proven to describe well a multitude of superconducting phenomena. Similar to the weak coupling is the “renormalized Bardeen–Cooper–Schrieffer (BCS)” model (Nicol and Carbotte, 2005) that incorporates the Eliashberg corrections in the effective coupling constants. We call our approach a “weak-coupling two-band scheme” and refer the reader to the original papers where it is clarified that the applicability of the model for the analysis of the superfluid density and specific heat data is broader than the traditional weak coupling (Kogan, 2002; Kogan et al., 2009). The Eilenberger approach can be used to describe the self-consistently two-gap situation, in which

$$\Delta(k) = \Delta_{1,2}, \quad k \in F_{1,2}, \quad (18.32)$$

where F_1, F_2 are two separate sheets of the Fermi surface. Denoting the densities of states on the two parts as $N_{1,2}$, we have for a quantity X constant at each Fermi sheet:

$$\langle X \rangle = \frac{X_1 N_1 + X_2 N_2}{N(0)} = n_1 X_1 + n_2 X_2, \quad (18.33)$$

where $n_{1,2} = N_{1,2}/N(0)$; clearly, $n_1 + n_2 = 1$.

The self-consistency Eq. (18.12) now takes the form:

$$\Delta_v = 2\pi T \sum_{\mu=1,2} n_\mu \lambda_{v\mu} f_\mu = \sum \mu n_\mu \lambda_{v\mu} \Delta_\mu \sum_{\omega} \frac{2\pi T}{\beta_\mu}, \quad (18.34)$$

where $v = 1, 2$ is the band index, and $\lambda_{v\mu} = N(0)V(v,\mu)$ are dimensionless effective interaction constants. Note that the notation commonly used in literature for $\lambda_{v\mu}^{(\text{lit})}$ differs from ours: $\lambda_{v\mu}^{(\text{lit})} = n_\mu \lambda_{v\mu}$

Turning to the evaluation of $\Delta_v(T)$, we note that the sum over ω in Eq. (18.34) is logarithmically divergent. To deal with this difficulty, we employ Eilenberger's idea of replacing h with the measurable T_c . Introducing dimensionless quantities

$$\delta_v = \frac{\Delta_v}{2\pi T} = \frac{\Delta_v}{T_c} \frac{1}{2\pi t'} \quad (18.35)$$

with $t = T/T_c$, we obtain:

$$\delta_v = \sum_{\mu=1,2} n_\mu \lambda_{v\mu} \delta_\mu \left(\tilde{\lambda} + \ln \frac{T_c}{T} - A_\mu \right), \quad (18.36)$$

$$A_\mu = \sum_{n=0}^{\infty} \left(\frac{1}{n + \frac{1}{2}} - \frac{1}{\sqrt{\delta_\mu^2 + (n + \frac{1}{2})^2}} \right). \quad (18.37)$$

$$1.76T_c = 2\hbar\omega_D \exp(-1\tilde{\lambda}), \quad (18.37a)$$

or

$$1\tilde{\lambda} = \ln \frac{T}{T_c} + \sum_{\omega}^{\omega D} \frac{2\pi T}{\hbar\omega}. \quad (18.38)$$

In terms of $\lambda_{v\mu}$, $\tilde{\lambda}$ is expressed as:

$$\tilde{\lambda} = \frac{2n_1 n_2 (\lambda_{11} \lambda_{22} - \lambda_{12}^2)}{n_1 \lambda_{11} + n_2 \lambda_{22} - \sqrt{(n_1 \lambda_{11} + n_2 \lambda_{22})^2 - 4n_1 n_2 \lambda_{12}^2}}. \quad (18.39)$$

For the given coupling constants $\lambda_{v\mu}$ and densities of states n_v , this system can be solved numerically for δ_v and therefore provide the gaps $\Delta_v = 2\pi T \delta_v(t)$. Example calculations are shown in Fig. 18.1. The first graph in the top row is calculated assuming no interband coupling. Naturally, we obtain material with two different transition temperatures. The second graph shows the gaps with $\lambda_{12} = 0.05$, which features a single T_c and a rather nonsingle-BCS-gap temperature dependence of the smaller gap. The single BCS gap is shown for comparison.

E. Superfluid density

Having formulated the way to evaluate (T) , we turn to the London penetration depth given for general anisotropies of the Fermi surface and of Δ by Eq. (18.23)

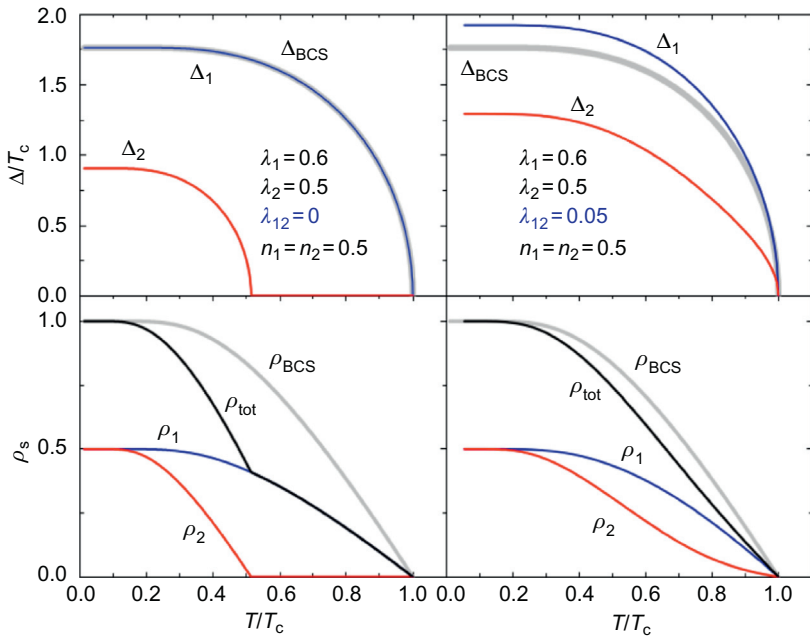


Figure 18.1 Top row: Self-consistent gaps calculated for the indicated $\lambda_{\nu\mu}$ in a compensated metal with $\mu = 1$. First graph is for no interband pairing, $\lambda_{12} = 0$, the second is for $\lambda_{12} = 0.05$. Bottom row: Corresponding partial and total superfluid densities.

(Kogan, 2002). We consider here only the case of currents in the a , b -plane of uniaxial or cubic materials with two separate Fermi surface sheets, for which the superfluid density, $\rho = \frac{\lambda_{ab}^2(0)}{\lambda_{ab}^2(T)}$, is:

$$\rho = \gamma\rho_1 + (1 - \gamma)\rho_2,$$

$$\rho_v = \delta_v^2 \sum_{n=0}^{\infty} \left[\delta_v^2 + \left(n + \frac{1}{2} \right)^2 \right]^{-\frac{3}{2}},$$

$$\gamma = \frac{n_1 v_1^2}{n_1 v_1^2 + n_2 v_2^2}, \quad (18.40)$$

where the v_ν^2 are the averages of the in-plane Fermi velocities over the corresponding band.

With the discovery of two-gap superconductivity in a number of materials, including MgB₂ (Bouquet et al., 2001; Fletcher et al., 2005), Nb₂Se (Fletcher, 2007), V₃Si (Nefyodov et al., 2005), Lu₂Fe₃Si₅ (Gordon et al., 2008), and ZrB₁₂

(Gasparov et al., 2006) one of the most popular approaches to analyze the experimental results has been the so-called “ α -model” (Bouquet et al., 2001). Developed originally to renormalize a single weak-coupling BCS gap to account for strong-coupling corrections (Padamsee et al., 1973), it was used to introduce two gaps, $\Delta_{1,2}$, each having a BCS temperature dependence but different amplitudes (Bouquet et al., 2001). This allowed for a simple way to fit the data on the specific heat (Bouquet et al., 2001) and the superfluid density, $\rho = x\rho_1 + (1+x)\rho_2$ (Prozorov and Giannetta, 2006; Fletcher et al., 2005). Here, $\rho_{1,2}$ are evaluated with $\Delta_{1,2} = (\alpha_{1,2}/1.76)\Delta_{\text{BCS}}(T)$, and x takes into account the relative band contributions. The fitting is usually quite good (thanks to a smooth and relatively “featureless” $\rho(T)$) and the parameters were found to be one larger and one smaller than unity (unless they are both equal to one in the single-gap limit). Although the α -model had played an important and timely role in providing convincing evidence for the two-gap superconductivity, it is *intrinsically inconsistent* as applied over the full temperature range. The problem is that we cannot assume *a priori* temperature dependencies for the gaps in the presence of however weak interband coupling (required to have single T_c). In the unlikely situation of zero interband coupling, two gaps would have single-gap BCS-like T dependencies but will have two different transition temperatures. The formal similarity in terms of additive partial superfluid densities prompted us to name our scheme the “ γ -model.” We note, however, that these models are quite different: our γ that determines partial contributions from each band is not just a partial density of states n_1 of the α -model; instead it involves the band’s Fermi velocities. The gaps, $\Delta_{1,2}(T)$, are calculated self-consistently during the fitting procedure.

The γ -models can be simplified for a compensated metal, such as the clean stoichiometric superconductor LiFeAs (Kim et al., 2011a,b). To reduce the number of fitting parameters, and yet capture compensated multiband structure, we consider a simplistic model of two cylindrical bands with the mass ratio, $\mu = m_1/m_2$, whence the partial density of states of the first band is $n_1 = \mu/(1+\mu)$. The total superfluid density is $\rho_s = \gamma\rho_1 + (1-\gamma)\rho_2$ with $\gamma = 1/(1+\mu)$. We also use the Debye temperature of 240 K (Wei et al., 2010) to calculate T_c , which allows fixing one of the in-band pairing potentials, λ_{11} . This leaves three free fitting parameters: the second in-band potential, λ_{22} ; the interband coupling, λ_{12} ; and the mass ratio, μ . Indeed, we found that $\rho_s(T)$ can be well described over the entire temperature range by this clean-limit weak-coupling BCS model (Kim et al., 2011a,b). Figure 18.2 shows the fit of the experimental superfluid density to the γ -model. The insets show temperature-dependent superconducting gaps obtained as a solution of the self-consistency equation, Eq. (18.34), and the lower inset shows the gap ratio as a function of temperature. Evidently, the smaller gap does not exhibit a BCS temperature dependence emphasizing the failure of the commonly used α -model.

Lastly, we note that in order to have two distinct gaps, as observed in many experiments (Johnston, 2010), we must have significant in-band coupling constants, λ_{11} and λ_{22} . To support this conclusion we calculate the gap ratio $\gamma_\Delta = \Delta_1(0)/\Delta_2(0)$ for fixed λ_{12} and varying λ_{11} and λ_{22} . The red lines in each graph of Fig. 18.3 show $\gamma_\Delta = 2$. For all cases, we need significant λ_{12} and varying λ_{11} to

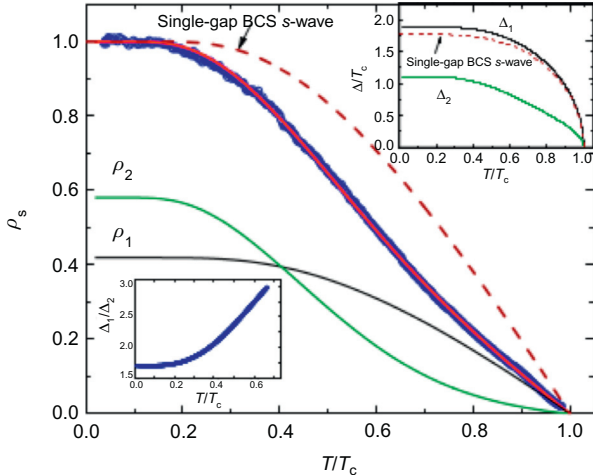


Figure 18.2 Symbols: Superfluid density, $\rho_s(T) = (\lambda(0)/\lambda(T))^2$, in a single crystal of LiFeAs calculated from the measured $\lambda(T)$ with $\lambda(0) = 200$ nm. Solid lines represent the fit to a two-gap γ -model, $\rho_s = \gamma\rho_1 + (1 - \gamma)\rho_2$. The dashed line is a single-gap BCS solution. Upper inset: Superconducting gaps, $\Delta_1(T)$ and $\Delta_2(T)$ calculated self-consistently during the fitting. Lower inset: Δ_1/Δ_2 as a function of temperature.

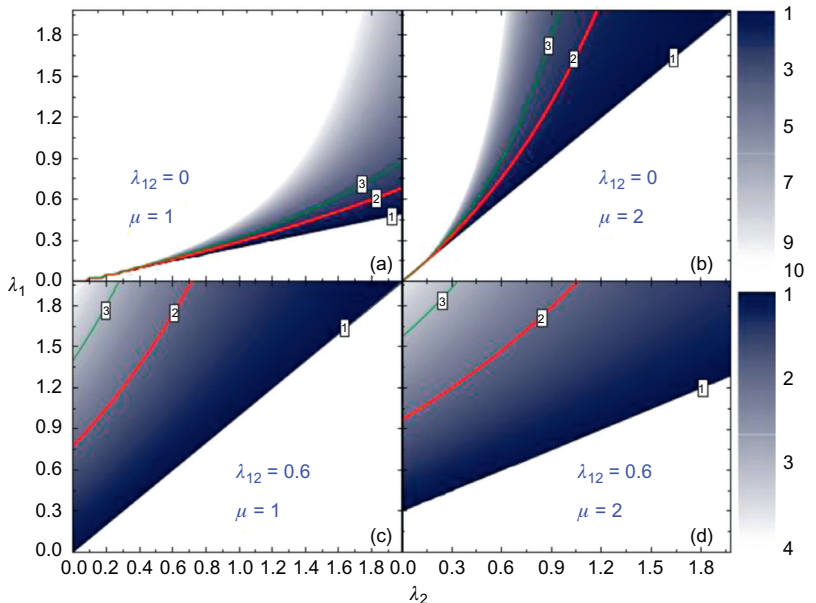


Figure 18.3 Gap ratio, $\gamma_\Delta = \Delta_1(0)/\Delta_2(0)$ for indicated μ (to check the effect of different partial densities of states) and λ_{12} . The magnitude of γ_Δ is given by the intensity shown on the right. Red lines in each graph show $\gamma_\Delta = 2$, which corresponds to the experimental situation in the pnictides.

reach this gap ratio. Therefore, the original simplified $s \pm$ model with two identical Fermi surfaces and only interband coupling, $\lambda_{12} \neq 0$ and $\lambda_{11} = \lambda_{22} = 0$ does not describe the experimentally found two distinct gaps in Fe-based superconductors (Mazin et al., 2008).

IV. Effects of scattering

The scattering by impurities strongly affects the London penetration depth λ even in the simplest case of nonmagnetic impurities in materials with an isotropic gap parameter and for scattering processes that can be characterized by the scalar (isotropic) scattering rate. The Δ anisotropy and the presence of magnetic impurities complicate the analysis of $\lambda(T)$, among other reasons, due to the T_c suppression in these cases. For an extended treatment, refer to Gordon et al. (2010) and Kogan (2009), whereas here we only summarize properties related to the discussion of our results. Introducing the nonmagnetic scattering rate, $1/\tau$, and the magnetic scattering rate (spin-flip), $1/\tau_m$, the London penetration depth λ is expressed as:

$$(\lambda^2)^{-1} = \frac{16\pi^2 e^2 T N(0) \langle v_i v_k \rangle}{c^2} \sum_{\omega} \frac{f_0^2}{\frac{\Delta}{f_0} + \frac{\hbar}{2\tau}}, \quad (18.41)$$

Here $1/\tau^{\pm} = 1/\tau \pm 1/\tau_m$. Clearly, the evaluation of $\lambda(T)$ in the presence of magnetic impurities is quite involved. However, there is one limit, for which we have a simple analytic answer, as discussed next.

A. Gapless limit

This is the case of τ_m close to $2\hbar/\Delta_0(0)$, the critical value for which $T_c = 0$; that is, $\tau_m \Delta \ll 1$. The resulting expression for the order parameter is remarkably simple (Abrikosov and Gor'kov, 1960):

$$\Delta^2 = 2\pi^2(T_c^2 - T^2). \quad (18.42)$$

The result for the superfluid density is valid over the entire temperature range, $T < T_c$.

$$\Delta^2 = 2\pi^2(T_c^2 - T^2), \quad (18.43)$$

where $\rho = \hbar/(2\pi T_c \tau)$, $\rho_m = \hbar/(2\pi T_c \tau_m)$ and $\rho^{\pm} = \rho \pm \rho_m$. For a short transport mean-free path $\rho \gg \rho_m$ we have the Abrikosov–Gor'kov result:

$$(\lambda^2)^{-1} = \frac{8\pi^3 e^2 N(0) \langle v_i v_k \rangle}{c^2 \rho \rho_m} (1 - t^2). \quad (18.44)$$

The idea of strong pair-breaking and, perhaps, gapless superconductivity finds experimental evidence in Fe-based superconductors in the form of scaling relations for the specific heat jump and a prefactor of the quadratic temperature variation of $\lambda(T)$ (Gordon et al., 2010; Kogan, 2009).

To summarize, in the case of superconductor with line nodes, impurity scattering will change the linear temperature dependence of the penetration depth at $T \ll T_c$ to become quadratic (Hirschfeld and Goldenfeld, 1993). Disorder will also lift the c -axis line nodes in the case of an extended s -wave, and induce a change from effective T^2 to exponentially activated behavior for the in-plane penetration depth (Mishra et al., 2009). However, if we start at the clean limit of a fully gapped superconductor and introduce pair-breaking scattering (either due to magnetic impurities or due to an unconventional gap structure such as s_{\pm} ; Mazin et al., 2008), the penetration depth will also exhibit a power-law behavior or approaching z variation in the gapless limit. Therefore, with increasing impurity scattering, if $\lambda(T) \sim T^n$, we expect the exponent n to change from 1 to 2 in the case of a nodal superconductor (or even from 1 to exponential in the case of nonsymmetry-imposed nodes) and from exponential to 2 for a fully gapped material with pair-breaking. This is schematically illustrated by the shaded areas in Fig. 18.10 (where we used large values of the exponent n to designate the exponential behavior).

V. Experimental results

The compound $\text{Ba}(\text{Fe}_{1-x}\text{T}_x)_2\text{As}_2$ is one of the most widely studied systems among all the iron-based superconductors, and we have collected extensive data that illustrate general features often common to many other members of the diverse pnictide family. Here we focus on electron-doped $\text{Ba}(\text{Fe}_{1-x}\text{T}_x)\text{As}_2$ with $\text{T} = \text{Co}$ and Ni . One reason why these series were chosen is because large, high-quality single crystals are available (Canfield and Bud'ko, 2010). All samples were grown from the self-flux and were extensively characterized by transport, structural, thermal, and magneto-optical analysis. They all exhibited uniform superconductivity at least at the $1 \mu\text{m}$ scale and dozens of samples were screened before entering into the resulting discussion (Canfield and Bud'ko, 2010; Ni et al., 2008a, b). To demonstrate the sample quality we show magneto-optical images in Figs. 18.4 and 18.5. Details of this visualization technique are described by us elsewhere (Prozorov et al., 2009b). In the images, the intensity is proportional to the local magnetic induction. All samples exhibit excellent Meissner screening (Prozorov et al., 2009b). Figure 18.4 shows the penetration of the magnetic field into the optimally doped sample with $x = 0.07$ at 20 K. A distinct “Bean oblique wedge” shape (Bean, 1964) of the penetrating flux with the current turn angle of 45° (implying an isotropic in-plane current density) is observed.

Furthermore, to look for possible mesoscopic faults and inhomogeneities, we show the trapped magnetic flux obtained after cooling in a 0.15 T magnetic field and turning the field off. The vortex distribution is quite homogeneous, indicating

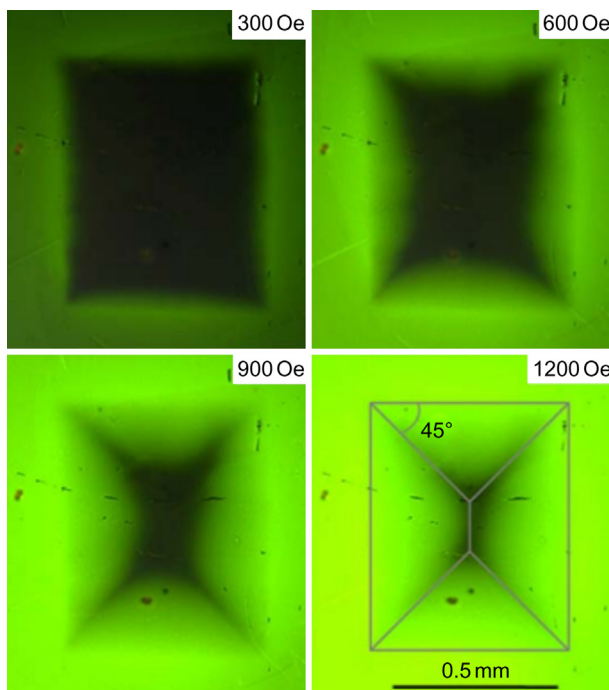


Figure 18.4 Magnetic flux penetration at 20 K into a $\text{Ba}(\text{Fe}_{0.93}\text{Co}_{0.07})_2\text{As}_2$ crystal. The last frame shows a schematic overlay of the expected “Bean oblique wedge” shape with isotropic in-plane current density.

robust uniform superconductivity for various doping levels. This is shown in Fig. 18.5 for four different doping levels.

The parent compound, BaFe_2As_2 , is a poor metal (Tanatar et al., 2009a, b) having a high temperature tetragonal phase with no long-range magnetic order, and it undergoes structural and magnetic transitions around 140 K into a low-temperature orthorhombic phase with long-range antiferromagnetic spin density wave order (Canfield and Bud’ko, 2010). Transition metal doping onto the iron site serves to suppress the structural and magnetic transition temperatures and superconductivity emerges after the magnetism has been sufficiently weakened. Doping into the barium site with potassium results in hole-doped superconductivity. Properties of this hole-doped system, at least as far as penetration depth is concerned, are quite similar to the electron-doped FeT122 (Hashimoto et al., 2009a, b; Martin et al., 2009a, b). On the other hand, the properties of materials obtained by isovalent doping of phosphorus into the arsenic site seems to induce superconductivity without introducing significant scattering, and seems to result in a superconducting gap with line nodes (Hashimoto et al., 2010).

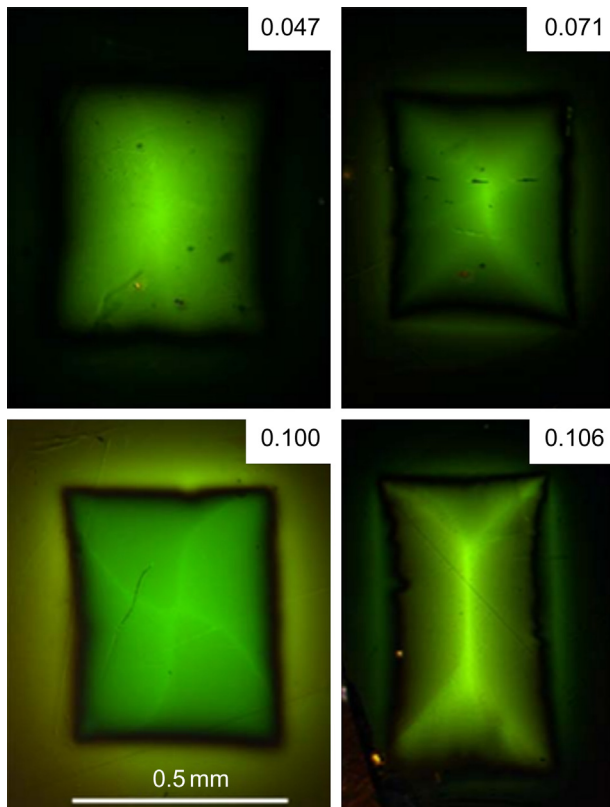


Figure 18.5 Magnetic flux trapped in samples after cooling in a 0.15 T magnetic field to 5 K and turning the field off. Doping levels, x , are indicated in right top corners.

In the charge-doped systems, angle-resolved spectroscopy (ARPES; Ding et al., 2008; Evtushinsky et al., 2009; Liu et al., 2009; Xu et al., 2011) and thermal conductivity (Tanatar et al., 2010; Reid et al., 2010) consistently show fully gapped Fermi surfaces (however with the gap anisotropy increasing upon departure from optimal doping in the case of thermal conductivity (Tanatar et al., 2010)). Furthermore, the c -axis behavior is quite different and it is possible that a nodal state develops upon doping beyond an optimal level (Martin et al., 2010a, b; Reid et al., 2010). The in-plane penetration depth consistently shows nonexponential power-law behavior (Williams et al., 2010; Luan et al., 2010, 2011; Prozorov et al., 2009a; Hashimoto et al., 2009a, b; Bobowski et al., 2010; Gordon et al., 2010; Martin et al., 2009a, b, 2010a, b; Gofryk et al., 2010; Gordon et al., 2009a, b; Kim et al., 2010; Prozorov et al., 2010a; Williams et al., 2009). It seems that such behavior can be explained by pair-breaking scattering (Bang, 2009; Dolgov et al., 2009; Senga and Kontani, 2008; Vorontsov et al., 2009). This is supported experimentally by the observed variation of the low-temperature $\lambda(T)$ within nominally the same

system (and even in pieces of the same sample; Hashimoto et al., 2009a, b), as well as deliberately introduced defects (Kim et al., 2010). In this chapter, we also discuss the case of a substantial variation of $\lambda(T)$ between various samples, probably due to edge effect.

In the following analysis, we use two ways to represent the power-law behavior: $\lambda(T) = \lambda(0) + A(T/T_c)^2$ at low temperatures (below $0.3T_c$) with A being the only free parameter, because at a gross level, all the samples follow the $\lambda(T) \sim T^2$ behavior rather well and $\lambda(T) = \lambda(0) + C/T^n$, leaving the exponent n as a free parameter to analyze its evolution with doping or artificially introduced defects. In the case of vertical line nodes, we expect a variation from $n = 1$ to $n = 2$ upon an increase of pair-breaking scattering (Hirschfeld and Goldenfeld, 1993), but in the case of a fully gapped s_{\pm} state we expect an opposite trend to approach $n = 2$ in the dirty limit from clean-limit exponential behavior (Bang, 2009; Dolgov et al., 2009; Senga and Kontani., 2008; Vorontsov et al., 2009). If, however, nodes are formed predominantly along the c -axis in the extended s -wave scenario, the effect of scattering on the in-plane penetration depth would be the opposite—starting from roughly $n = 2$ in the clean limit and approaching exponential in the dirty limit (Mishra et al., 2011).

A. In-plane london penetration depth

Figure 18.6 shows the normalized differential TDR magnetic susceptibility of several single crystals of $\text{Ba}(\text{Fe}_{1-x}\text{Co}_x)_2\text{As}_2$ across the superconducting “dome.” All but one sample was grown at the same conditions and with similar starting chemicals. All but one had thicknesses in the range of 100–400 nm. One of the samples ($x = 0.074$, denoted batch #2) was cleaved for the irradiation experiments and had a

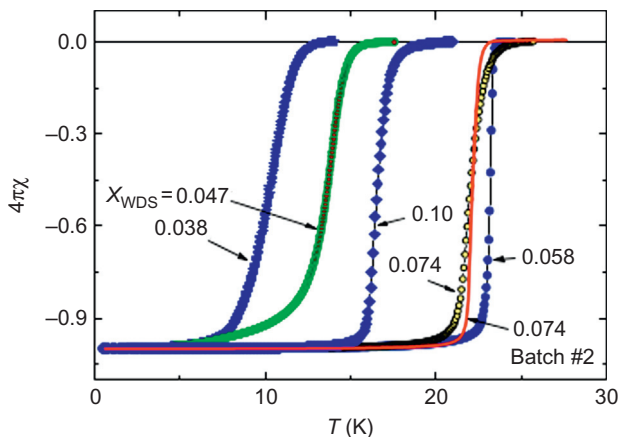


Figure 18.6 $4\pi\chi(T)$ in single crystals of $\text{Ba}(\text{Fe}_{1-x}\text{Co}_x)_2\text{As}_2$ for different x . Sample from batch #1 is indicated by a solid line.

thickness of 20 nm. We used it for comparison with the “thick” batch #1 and also to study the effects of deliberately induced defects. It turns out that the edges of the thicker samples are not quite smooth and, when imaged in scanning electron microscope (SEM), look like a used book (see Fig. 18.11a). Since calibration of the TDR technique relies on the volume penetrated by the magnetic field, the thinner samples should be closer to the idealization of the sample geometry (top and bottom surfaces are always very flat and mirror-like), thus producing a more reliable calibration. On the other hand, this would only lead to a change of the amplitude (due to geometric miscalibration) of the penetration depth variation (i.e., prefactor A) and would not change its functional temperature dependence (i.e., the exponent n). Thinner samples, on the other hand, have better chances to be more chemically uniform, and hence have reduced scattering. We observed these effects by comparing samples from different batches.

The low-temperature variation of the London penetration depth is presented in Fig. 18.7 as a function of $(T/T_c)^n$ obtained by fitting the data to $\Delta\lambda(T) = \lambda(0) + C(T/T_c)^n$. Each curve reveals a robust power-law behavior with the exponent n shown in the inset in Fig. 18.7. The fitted exponent n varies from $n = 2 \pm 0.1$ for underdoped samples to $n = 2.5 \pm 0.1$ for the overdoped samples within the batch #1 and reaches $n = 2.83$ in batch #2. If the superconducting density itself follows a power law with a given n , then $C \sim f_s(c/\omega_\rho)S$, where f_s is the superconducting fraction at zero temperature, c is the speed of light, S is defined by the fraction of the Fermi surface that is gapless (which may reflect a multigap character of the superconductivity, possible nodal structure, unitary impurity scattering strength, etc.), and ω_ρ is the plasma frequency.

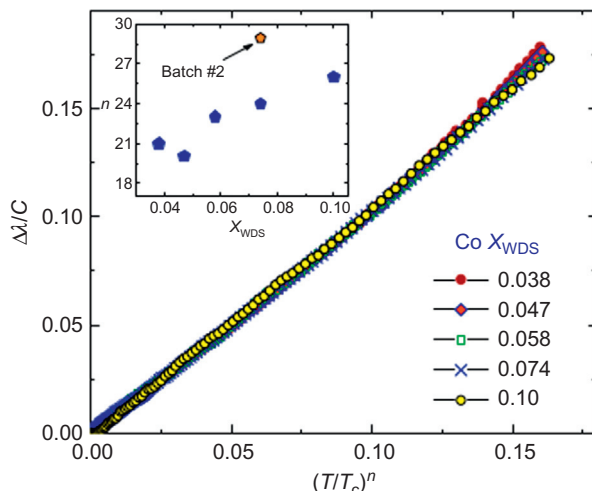


Figure 18.7 Low-temperature behavior of $\Delta\lambda(T)$ versus $(T/T_c)^n$ for all studied concentrations. Inset shows exponent n as function of concentration. Sample from batch #2 is shown for comparison.

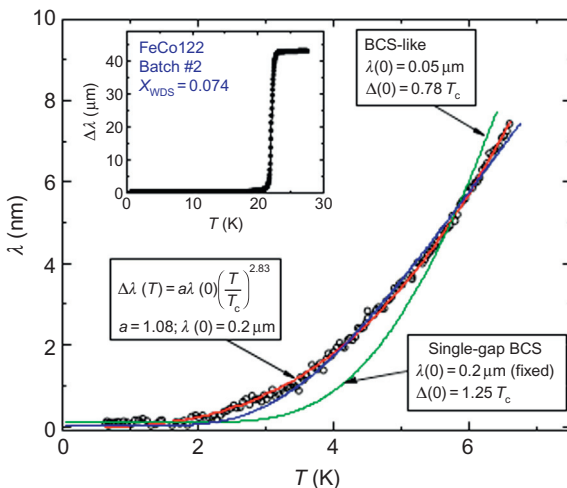


Figure 18.8 Low-temperature behavior of $\Delta\lambda(T)$ for the sample batch #2. Solid lines are fits to three functions described in the text. Inset shows full temperature variation indicating a very sharp superconducting transition.

Clearly the sample of batch #2 shows a behavior much closer to exponential compared to batch #1. As discussed earlier, this could be due to the variation of scattering between the batches. We analyze low-temperature $\lambda(T)$ in Fig. 18.8. We attempted to fit the data with three functions: the power-law with free prefactor C and exponent n , the standard single-gap BCS behavior, Eq. (18.27), with a fixed value of $\lambda(0) = 200$ nm and $\Delta(0)$ as a free parameter, and to a BCS-like function where both $\lambda(0)$ and $\Delta(0)$ are free parameters. The resulting values are shown in Fig. 18.8. The power-law fit yields a quite high exponent $n \approx 2.83$ and the best fit quality. The BCS-like fit yields a reasonable fit quality but produces unrealistic values of both $\lambda(0) \approx 48$ nm and $\Delta(0) \approx 0.78T_c$ (the latter cannot be less than a weak-coupling BCS value of 1.76). Finally, the fixed $\lambda(0)$ BCS fit does not agree with the data and also produces unreasonable $\Delta(0) \approx 1.25T_c$. One firm conclusion follows from this exercise—we are dealing with a multigap superconductor.

In order to understand the validity of the empirical power-law behavior, Fig. 18.9 shows low-temperature behavior of $\Delta\lambda(T)$ versus $(T/T_c)^{2.83}$ for the sample from batch #2. Arrows indicate the actual reduced temperature. The inset zooms at below the commonly accepted “low-temperature limit” of $\approx T_c/3$. Clearly, power-law behavior is robust and persists down to the lowest temperature of the experiment of $T \approx 0.02 T_c$.

We now summarize the observed power-law behavior of the in-plane penetration depth for the electron-doped 122 family of superconductors. Figure 18.10 shows the experimental low-temperature limit power-law exponent for different dopants at the Fe site and for different doping regimes. The shaded areas show the expectations for the pair-breaking scattering effects in s - and d -wave scenarios. It seems that

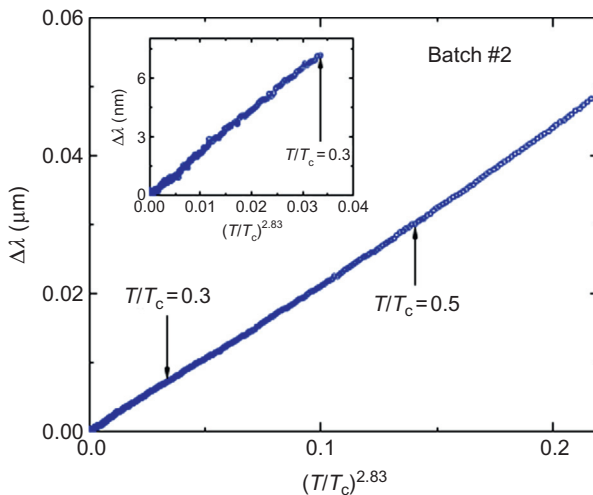


Figure 18.9 Low-temperature behavior of $\Delta\lambda(T)$ versus $(T/T_c)^{2.83}$ for the sample from batch #2. Marks show actual reduced temperature. Insets show the behavior below the commonly accepted “low-temperature limit” of $\approx T_c/3$.

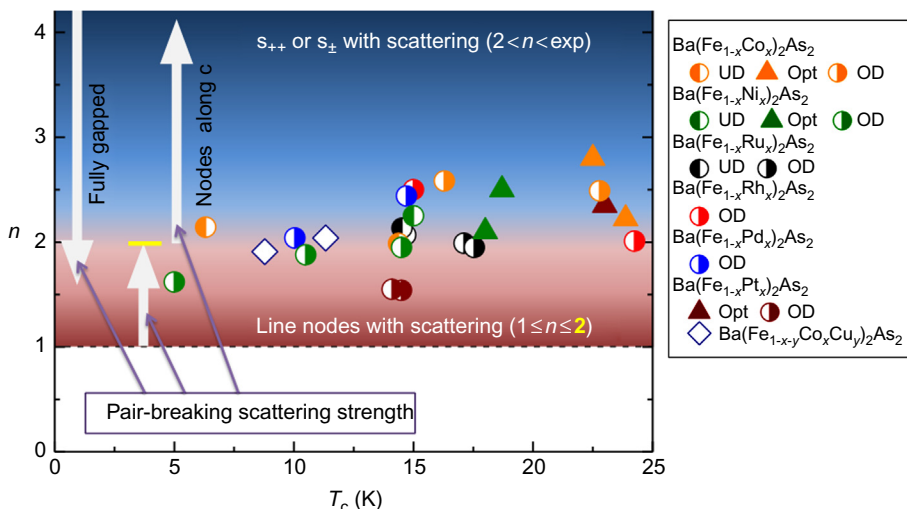


Figure 18.10 Power-law exponent of the low-temperature variation of in-plane $\lambda_{ab}(T)$ in several electron-doped Ba122 superconductors at various doping levels. Shaded areas show the influence of pair-breaking scattering with $n = 2$ being the limiting value of n approaching from either the s -wave side (nodeless exponential) or d -wave side (vertical line nodes). In the case of extended s -wave with nodes predominantly along the c -axis, effective n increases from 2 in the clean limit toward the exponential behavior when the nodes are lifted by scattering.

statistically d -wave pairing (more generally, vertical line nodes) cannot explain the in-plane variation of the penetration depth. However, if the nodes appear somewhere predominantly along the c -axis, they may induce an apparent power-law behavior of $\lambda_{ab}(T)$ with the effective $n \approx 2$ in the clean limit and going toward exponential behavior with the increase of the scattering rate (Mishra et al., 2011).

B. Absolute value of the penetration depth

To further investigate the effects of doping and the difference between the batches, we use the method described in Section II.A, which involves measuring the sample, coating it with a uniform layer of Al, and remeasuring (Gordon et al., 2010; Prozorov et al., 2000b). The Al film was deposited onto each sample while it was suspended from a rotating stage by a fine wire in the argon atmosphere of a magnetron sputtering system. The film thickness was checked using an SEM in two ways, both of which are shown in Fig. 18.11. The first method involved breaking a coated

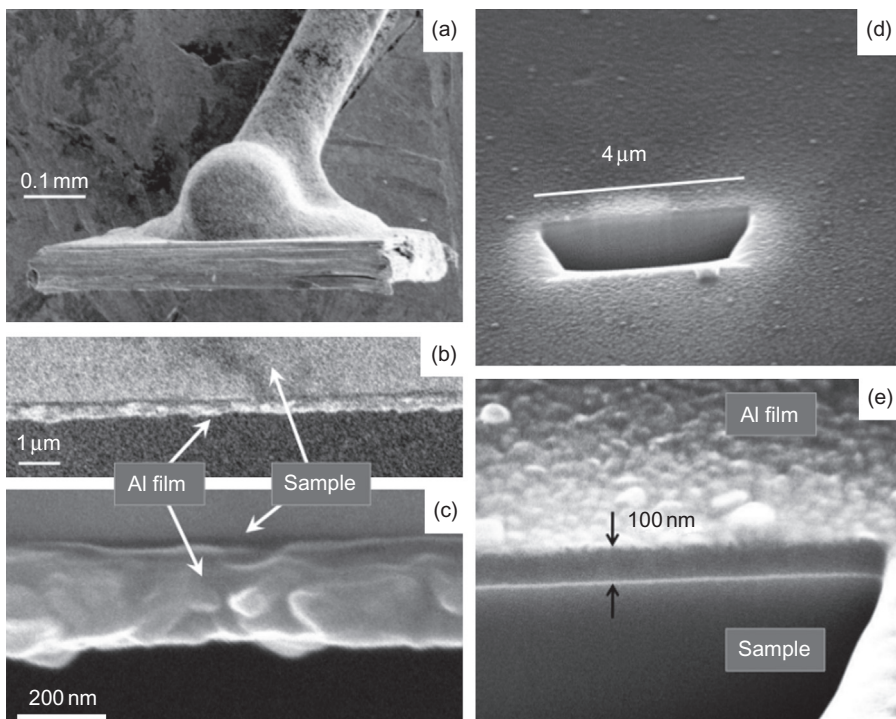


Figure 18.11 SEM images of the Al-coated samples. (a) Large-scale view. The broken side is on top, (b) and (c) are zoomed in on the Al film on the edge of the broken side. (d) A trench produced by an FIB. (e) Close-up view of the FIB trench showing the Al film and its thickness.

sample after all measurements had been performed to expose its cross section. After this, it was mounted on an SEM sample holder using silver paste, shown in Fig. 18.11a. The images of the broken edge are shown for two different zoom levels in Fig. 18.11b and c. The second method used a focused ion beam (FIB) to make a trench on the surface of a coated sample, with the trench depth being much greater than the Al coating thickness, shown in Fig. 18.11d. The sample was then tilted and imaged by the SEM that is built into the FIB system, shown in Fig. 18.11e.

Examples of the penetration depth measurements before and after coating are shown in Fig. 18.12. Notice how small the effect of Al coating is when presented on a large scale of a full superconducting transition of the coated sample. However, the TDR technique is well suited to resolve the variation due to the aluminum layer (Gordon et al., 2010; Prozorov et al., 2000b). Obtained values of $\lambda_{ab}(0)$ are summarized in the top panel of Fig. 18.13 for doping levels, x , across the superconducting region of the phase diagram, shown schematically in the bottom panel of Fig. 18.13. The sizes of the error bars for the $\lambda_{ab}(0)$ points were determined by considering the film thickness to be $t = 100 \pm 10$ nm and $\lambda_{Al}(0) = 50 \pm 10$ nm. The scatter in the $\lambda_{ab}(0)$ values shown in the upper panel of Fig. 18.13 has an approximately constant value of ± 0.075 μm for all values of x , which probably indicates that the source of the scatter is the same for all samples. For comparison, Fig. 18.13 also shows $\lambda_{ab}(0)$ obtained from μSR measurements (red stars; Williams et al., 2010), the (MFM) technique (open stars; Luan et al., 2010, 2011), and optical reflectivity (purple open triangles; Nakajima et al., 2010). Given a statistical uncertainty these measurements

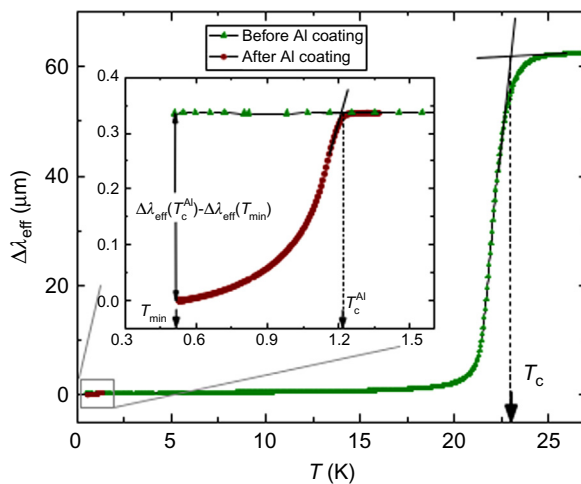


Figure 18.12 Main frame: Full superconducting transition of an optimally doped FeCo122 crystal from batch #1 before and after Al coating. Inset: Zoomed in low-temperature region, $T_{\min} \leq T \leq T_c^{\text{Al}}$, before (green triangles) and after (brown circles) the Al coating on the same sample. (Notice how small the effect on a full scale of the main frame is.)

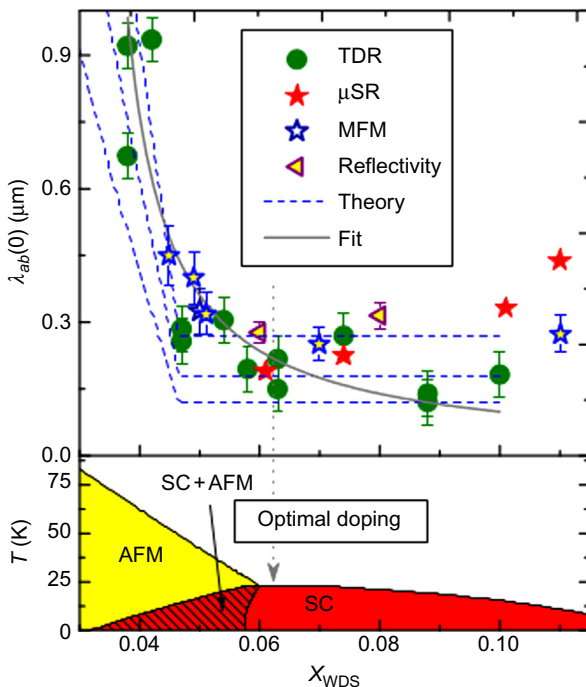


Figure 18.13 Top panel: The zero temperature London penetration depth, $\lambda_{ab}(0)$, as a function of the Co concentration, x . The three dashed blue lines are theoretical curves obtained using Eq. (18.45) for three different values of $\lambda_{ab}(0)$ in the pure superconducting state. The solid gray line is a fit to the TDR data only of the form $A + B/x^n$. Also shown are values of $\lambda_{ab}(0)$ obtained by other experiments for comparison explained in the text. Bottom panel: Schematic phase diagram for FeT122 system showing the coexisting region (Fernandes et al., 2010; Nandi et al., 2010).

are consistent with our results within the scatter. It may also be important to note that the $\lambda_{ab}(0)$ values from other experiments are all on the higher side of the scatter that exists within the TDR $\lambda_{ab}(0)$ data set. As discussed earlier, our TDR techniques give a low bound of $\lambda(0)$, consistent with this observation.

In order to provide a more quantitative explanation for the observed increase in $\lambda_{ab}(0)$ as x decreases in the underdoped region, we have considered the case of s^\pm superconductivity coexisting with itinerant antiferromagnetism (Fernandes et al., 2010). For the case of particle-hole symmetry (nested bands), the zero temperature value of the in-plane penetration depth in the region where the two phases coexist is given by Gordon et al. (2010) and Fernandes et al. (2010):

$$\lambda_{ab}^{\text{SC+SDW}}(0) = \lambda_{ab}^0(0) \sqrt{1 + \frac{\Delta_{\text{AF}}^2}{\Delta_0^2}} \quad (18.45)$$

where $\lambda_{ab}^0(0)$ is the value for a pure superconducting system with no magnetism present, and Δ_{AF} and Δ_0 are the zero temperature values of the antiferromagnetic and superconducting gaps, respectively. Deviations from particle-hole symmetry lead to a smaller increase in $\lambda_{ab}^{SC+SDW}(0)$, making the result in Eq. (18.45) an upper estimate (Fernandes et al., 2010).

The three blue dashed lines shown in the top panel of Fig. 18.13, which were produced using Eq. (18.45), show the expected increase in $\lambda_{ab}(0)$ in the region of coexisting phases below $x \approx 0.047$ by normalizing to three different values of $\lambda_{ab}(0)$ in the pure superconducting state, with those being 120, 180, and 270 nm to account for the quite large dispersion of the experimental values. This theory does not take into account changes in the pure superconducting state, so for $x > 0.047$ the dashed blue lines are horizontal. These theoretical curves were produced using parameters that agree with the phase diagram in the bottom panel of Fig. 18.13 (Fernandes et al., 2010; Nandi et al., 2010). While the exact functional form was not provided by any physical motivation and merely serves as a guide to the eye, the solid gray line in Fig. 18.13 is a fit of the TDR $\lambda_{ab}(0)$ data to a function of the form $A + B/x^n$, which does indeed show a dramatic increase of $\lambda_{ab}(0)$ in the coexistence region and also a relatively slight change in the pure superconducting phase. It should be noted that a dramatic increase in $\lambda_{ab}(0)$ below $x \approx 0.047$ cannot be explained by the impurity scattering, which would only lead to relatively small corrections in $\lambda(T)$.

With the experimental values of $\lambda(0)$ we can now analyze the superfluid density. In general, $\lambda^{-2}(T)$ is given by Eq. (18.23) and depends on the averaging over the particular Fermi surface; for example, in the simplest cylindrical case, Eq. (18.30) and $\lambda^{-2}(T) = 4\pi e^2 N(0)v^2/c^2$, where $N(0)$ is the density of states at the Fermi level and v is Fermi velocity. However, it is instructive to analyze the behavior from a two-fluid London theory point of view looking at the density of superconducting electrons, $n_s = (mc^2/4\pi e^2)\lambda^{-2}$ as a function of temperature. The zero value, $n_s(0)$, will in general be less than the total density of electrons due to pair-breaking scattering, so the magnitude is useful when comparing different samples.

Figure 18.14 shows the data for underdoped, optimally doped, and overdoped samples from batch #1 and also a sample from batch #2 for comparison. For this sample #2, $\lambda(0) = 200$ nm was used. There is a clear, but expected, asymmetry with respect to doping. Underdoped samples show quite low density, because not all electrons are participating in forming the Cooper pairs and parts of the Fermi surface are gapped by the Spin Density Wave (SDW) as was discussed earlier. The overdoped sample, $x = 0.01$, despite having smaller T_c than the ones with $x = 0.074$, shows the highest n_s . Obviously, the data scatter is significant. Therefore, the only reliable conclusion is that penetration depth increases dramatically upon entering the coexisting region. The overdoped side needs more study to acquire enough statistics. Furthermore, comparing two samples with $x = 0.074$ from two different batches reveals an even more striking difference. Not only does the sample from batch #2 have larger n , but the temperature dependence of ρ_s in the full temperature range is also quite different.

The pronounced convex shape (positive curvature) of $\rho_s(T)$ observed in all samples from batch #1 at elevated temperatures becomes much less evident in sample #2. The bottom panel of Fig. 18.14 clearly demonstrates this difference, which is

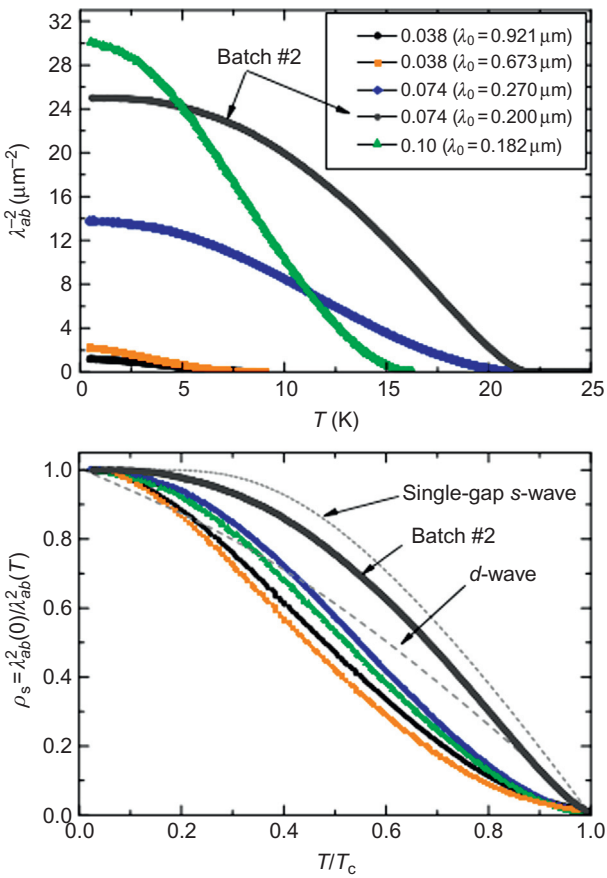


Figure 18.14 Top panel: $\lambda^{-2} \propto n_s$ versus T for underdoped, optimally doped, and overdoped concentrations for batch #1. A sample from batch #2 is shown for comparison. Bottom panel: Normalized superfluid density, $\rho_s \equiv n_s(T)/n_s(0) = (\lambda(0)/\lambda(T))^2$.

hard to understand based purely on the geometrical consideration (different thicknesses). It seems that thicker samples of batch #1 had a higher chance of being chemically inhomogeneous across the layers. On the other hand, the convex shape of $\rho_s(T)$ at elevated temperatures is a sign of the two-gap superconductivity (Kogan et al., 2009), which depends sensitively on the interaction matrix, $\lambda_{\nu\mu}$; see Section 3.2 and Eq. (18.34). This feature becomes more pronounced when the interband coupling, λ_{12} , becomes smaller compared to the in-band coupling potentials, λ_{11} and λ_{22} . If our interpretation that the difference between $x = 0.074$ samples from batch #1 and batch #2 is due to enhanced pair-breaking scattering in #1, this would indicate that this *scattering* is primarily of interband character, so it disrupts the *interband pairing*. Additional information regarding the role of scattering in determining the anomalous convex behavior was obtained from the microwave cavity perturbation

measurements on $\text{FeSe}_{0.4}\text{Te}_{0.6}$ single crystals (Takahashi et al., 2011). Both real and imaginary parts of the complex conductivity allowed a determination of $\lambda(T)$ and temperature-dependent scattering time from which a crossover from dirty to the clean limit upon cooling has been proposed. All these results provide an indirect leverage to the s_{\pm} scenario where interband coupling plays the major role.

The normalized superfluid density for sample #2 is analyzed in Fig. 18.15 by using a two-band γ -model described in Section III.B. Symbols show the data and the solid lines represent partial, $\rho_1(T)$ and $\rho_2(T)$, as well as total $\rho_s(T)$ obtained from the fit using Eq. (18.40). The fit requires solving the self-consistent coupled “gap” equations (18.36), which are shown in the inset in Fig. 18.15. Parameters of the fit are as follows: $\lambda_{11} = 0.80$, $\lambda_{22} = 0.49$, $\lambda_{12} = 0.061$, and $\gamma = 0.87$. We used a Debye temperature of 250 K (Johnston, 2010) to obtain the correct T_c via Eq. (18.37) that fixed λ_{11} and gave $\tilde{\lambda} = 0.41$. We also assumed equal partial densities of states on the two bands, so the value of $\gamma = 0.87$ most likely comes from the difference in the k -dependent Fermi velocities, but may also reflect the fact that densities of states are not equal. Indeed, presented fitting parameters should not be taken too literally. The superfluid density is calculated from the temperature-dependent gaps (inset in Fig. 18.15), and close temperature dependencies can be obtained with quite different fitting parameters. However, the gaps fully determine the experimental ρ_s and this is the main result. We find that $\Delta_1(0) = 1.883T_c = 3.73$ meV and $\Delta_2(0) = 0.754T_c = 1.49$ meV, which are in good agreement with specific heat (Gofryk et al., 2010; Hardy et al., 2010) and μ SR penetration depth measurements

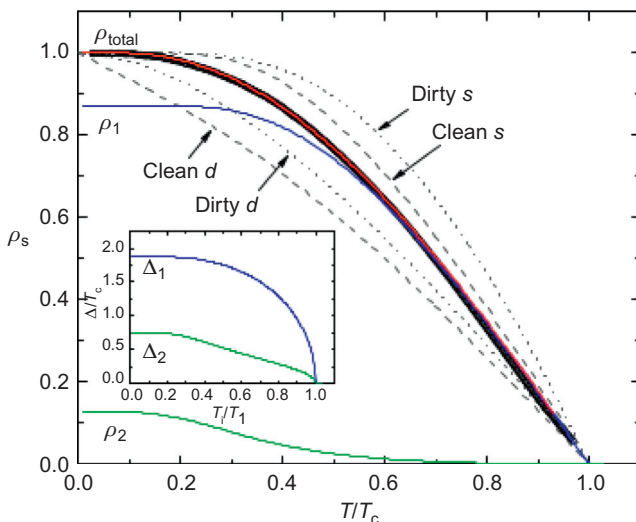


Figure 18.15 Normalized superfluid density for sample #2. Symbols show the data and the solid lines represent partial and total $\rho(T)$ obtained from a fit to Eq.(18.40) Also shown are the clean (dashed gray lines) and dirty (dotted gray lines) single-gap s - and d -wave cases. Inset shows superconducting gaps obtained self-consistently during the fitting; see Eq.(18.36).

(Williams et al., 2009) done on the samples of similar composition. Also shown in Fig. 18.15 are the clean (dashed gray lines) and dirty (dotted gray lines) single-gap *s*- and *d*-wave cases. (Note that although the gap does not depend on the nonmagnetic impurities in the isotropic *s*-wave case (Anderson theorem), the superfluid density does.) Clearly, $\rho_s(T)$ for sample 2 (and, of course for samples of batch #1) does not come even close to any of these single-gap scenarios.

C. Anisotropy of London penetration depths

Let us now discuss the electromagnetic anisotropy in the superconducting state, parameterized by the ratio $\gamma_\lambda = \lambda_c/\lambda_{ab}$. To determine λ_c we used the method described in Section II.C; the results are presented in Fig. 18.16. The problem is that we do not know the absolute value of $\lambda_c(0)$, so we could obtain $\Delta\lambda_c(T)$ only with the help of knowing $\Delta\lambda_{ab}(T)$, which was measured on the same crystal independently. To find the total $\lambda_c(T)$ we use the fact that close to T_c (in the region of validity of Ginzburg–Landau theory), we should have (Kogan, 2002):

$$\gamma\lambda(T_c) = \sqrt{\gamma_\rho(T_c)}, \quad (18.46)$$

where anisotropy of normal state resistivity, $\gamma_\rho = \rho_c/\rho_{ab}$, is taken right above T_c , with $\gamma_\rho \approx 4 \pm 1$ (Tanatar et al., 2009a, b), so that $\gamma_\lambda T_c \approx 2$. The results are shown in the inset in Fig. 18.16. Of course, there is some ambiguity in determining the exact anisotropy value, but the qualitative behavior does not change—the anisotropy increases upon cooling. With our estimate it reaches a modest value of 5 at low temperatures, which makes pnictides differ considerably from high- T_c cuprates.

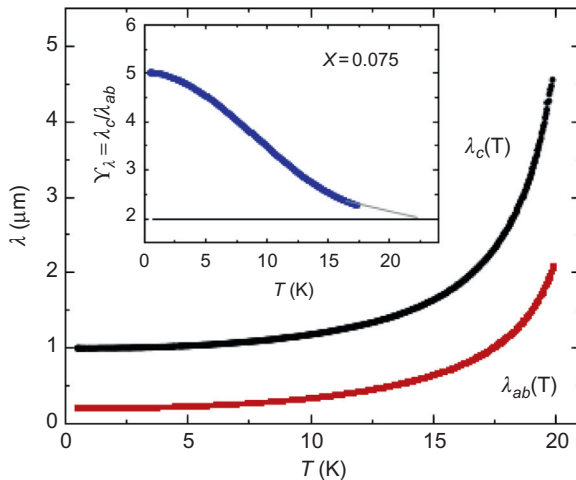


Figure 18.16 In-plane, $\lambda_{ab}(T)$, ***and out-of-plane, $\lambda_c(T)$, in a single crystal of FeCo122 with $x = 0.075$. Inset: Temperature-dependent anisotropy, $\gamma_\lambda = \lambda_c/\lambda_{ab}$.

This is opposite to a two-gap superconductor MgB₂ where γ_λ decreases upon cooling (Tanatar et al., 2009a, b), which may be due to a different dimensionality of the Fermi sheets. In any case, temperature-dependent γ_λ can only arise in the case of a multigap superconductor.

Next we examine the anisotropy of $\lambda(T)$ at different doping levels. This study was performed on FeNi122 samples and is reported in detail elsewhere (Martin et al., 2010a, b). Figure 18.17a summarizes the $T(x)$ phase diagram showing the structural/magnetic (T_{sm}) and superconducting (T_c) transitions. The inset shows TDR measurements in a full temperature range for all concentrations used in this study. Figure 18.17b shows the low-temperature ($T \leq 0.3T_c$) behavior of $\lambda_{ab}(T)$ for

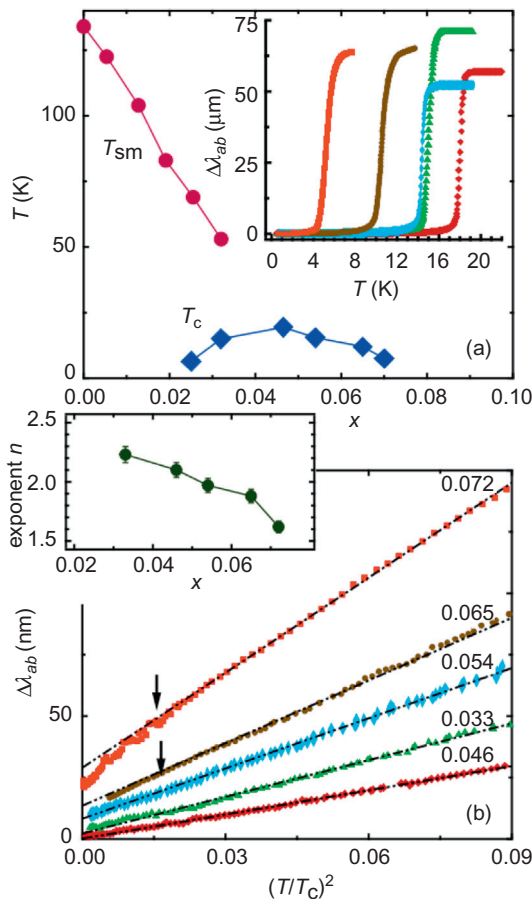


Figure 18.17 (a) Temperature-doping phase diagram of Ba(Fe_{1-x}Ni_x)₂As₂. The inset shows full temperature range superconducting transitions. (b) $\Delta\lambda_{ab}(T)$ for different doping levels versus $(T/T_c)^2$. The curves are shifted vertically for clarity. The inset shows the power-law exponent $n(x)$ obtained by fitting to $\lambda_{ab}(T) = a + bT^n$ from the base temperature up to $T/T_c = 0.3$.

several Ni concentrations. The data plotted versus $(T/T_c)^2$ are linear for underdoped compositions and show a clear deviation toward a smaller power-law exponent (below temperatures marked by arrows in Fig. 18.17b) for overdoped samples. While at moderate doping levels the results are fully consistent with our previous measurements in FeCo122 (Gordon et al., 2009a, b), the behavior in the overdoped samples is clearly less quadratic. It should be noticed that in order to suppress T_c by the same amount, we need a Ni concentration two times lower than Co. In previously FeCo122 (Gordon et al., 2009a), the samples never reached highly overdoped compositions equivalent to $x = 0.072$ of Ni shown in Fig. 18.17b. Therefore, Ni doping has the advantage of spanning the phase diagram with smaller concentrations of dopant ions, which may act as the scattering centers. The evolution of the exponent n with x is summarized in the lower inset in Fig. 18.17.

Now we apply a technique described in Section II.C to estimate $\lambda_c(T)$. Figure 18.18 shows the effective penetration depth, λ_{mix} (see Eq. (18.8)), for overdoped, $x = 0.072$ (main panel), and underdoped, $x = 0.033$ (inset), samples before (A) and after (B) cutting in half along the longest side (l -side) as illustrated schematically at the top of the figure. Already in the raw data, it is apparent that the

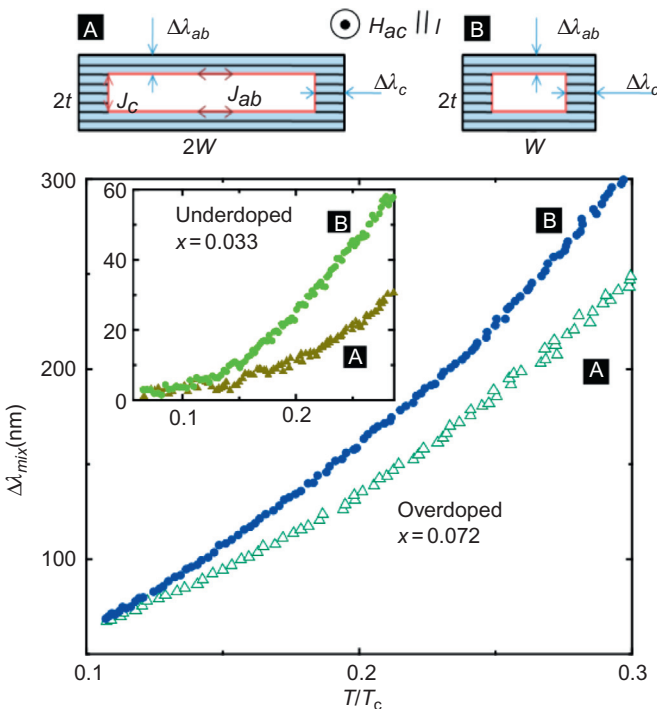


Figure 18.18 Schematics of magnetic field penetration in the case of $H_{ac} \parallel l$ for the whole sample (A) and after cutting in half along length l (B). (Main panel) The mixed penetration depth $\Delta\lambda_{\text{mix}}$ (T) before (A) and after (B) cutting for the overdoped sample $x = 0.072$, $T_c = 7.5$ K. Inset shows similar data for the underdoped $x = 0.033$, $T_c = 15$ K.

overdoped sample exhibits a much smaller exponent n compared to the λ_{ab} , while underdoped samples show a tendency to saturate below $0.13T_c$. Using Eq. (18.8) we can now extract the true temperature-dependent $\Delta\lambda_c(T)$. The result is shown in Fig. 18.19 for two different overdoped samples of the same composition, $x = 0.072$ having $T_c = 7.5$ K and $T_c = 6.5$ K, and for an underdoped sample with $x = 0.033$ having $T_c = 15$ K. Since the thickness of the sample is smaller than its width, we estimate the resolution of this procedure for $\Delta\lambda_c$ to be about 10 nm, which is much lower than 0.2 nm for $\Delta\lambda_{ab}$. Nevertheless, the difference between the samples is obvious. The overdoped samples show a clear linear temperature variation up to $T_c/3$, strongly suggesting nodes in the superconducting gap. The average slope is large, about $d\lambda_c/dT \approx 300$ nm/K indicating a significant amount of thermally excited quasiparticles. By contrast, in the underdoped sample the interplane penetration depth saturates, indicating a fully gapped state. If fitted to the power-law the exponent in the underdoped sample is $2 \leq n \leq 3$, depending on the fitting range.

Nodes, if present somewhere on the Fermi surface, affect the temperature dependence of both components of $\Delta\lambda(T)$. However, the major contribution still comes from the direction of the super current flow, thus placing the nodes in the present case at or close to the poles of the Fermi surface. The nodal topologies that are consistent with our experimental results are latitudinal circular line nodes located at the finite k_z wave vector or a point (or extended area) polar node with a nonlinear ($(\theta) \sim \theta^p$, $p > 1$) variation of the superconducting gap with the polar angle, θ . It is interesting to note a close similarity to the results of thermal conductivity measurements in overdoped FeCo122 that have reached the same conclusions—in-plane state is anisotropic, but nodeless (Tanatar et al., 2010), whereas the out-of-plane response

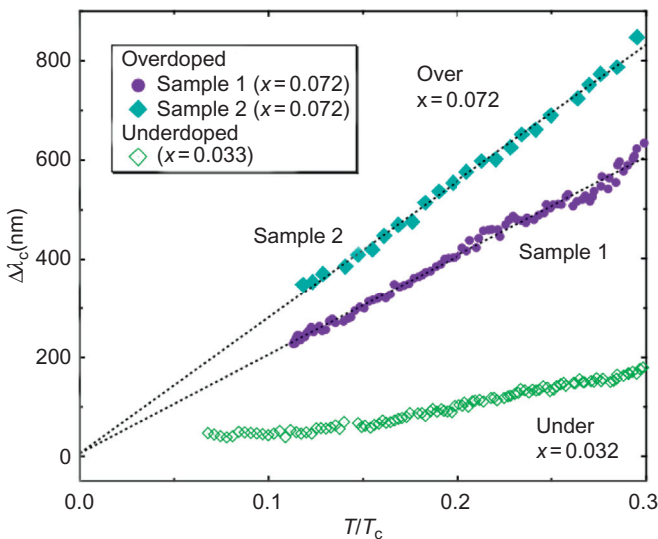


Figure 18.19 $\Delta\lambda_c(T)$ for the underdoped, $x = 0.033$, $T_c = 15$ K (under), and for two overdoped, $x = 0.072$, $T_c = 7.5$ K (over), and $T_c = 6.5$ K (over), samples. Dashed lines are linear fits.

is nodal (Reid et al., 2010). Still, we emphasize that the apparent power-law behavior of the in-plane penetration depth, $\lambda_{ab}(T)$, in heavily overdoped samples could be induced by the out-of-plane nodes (Graser et al., 2010). To summarize, it appears that not only is the gap not universal across different pnictide families (Hashimoto et al., 2010), it is not universal even within the same family over an extended doping range. Similar conclusions have been reached for the hole-doped BaK122 pnictides (Thomale et al., 2011; Kim et al., 2011a,b; Reid et al., 2011).

D. Pair-breaking

Although the natural variation in the scattering rates between samples provides a good hint toward the importance of pair-breaking scattering, for more quantitative conclusions we need to introduce further disorder. This can be achieved with the help of heavy-ion irradiation. To examine the effect of irradiation, $\sim 2 \times 0.5 \times 0.02\text{--}0.05 \text{ mm}^3$ single crystals were selected and then cut into several pieces preserving the width and the thickness. We compare sets of samples, where the samples in each set are parts of the same original large crystal and had identical temperature-dependent penetration depth in the unirradiated state. (These samples constitute what we call batch #2 in this review with unirradiated reference piece appearing in the discussion and figures of the previous sections.) Irradiation with 1.4 GeV $^{208}\text{Pb}^{56+}$ ions was carried out at the Argonne Tandem Linear Accelerator System (ATLAS) with an ion flux of $\sim 5 \times 10^{11} \text{ ions s}^{-1} \cdot \text{m}^{-2}$. The actual total dose was recorded in each run. Such irradiation usually produces columnar defects or the elongated pockets of disturbed superconductivity along the ions propagation direction. The density of defects, d , per unit area is usually expressed in terms of so-called “matching field,” $B_\phi = \Phi_0 d$, which is obtained assuming one flux quantum, $\Phi_0 \approx 2.07 \times 10^{-7} \text{ G cm}^2$ per ion track. Here we studied samples with $B_\phi = 0.5, 1.0$, and 2.0 T corresponding to $d = 2.4 \times 10^{10} \text{ cm}^{-2}, 4.8 \times 10^{10} \text{ cm}^{-2}$, and $9.7 \times 10^{10} \text{ cm}^{-2}$. The sample thickness was chosen in the range of $\sim 20\text{--}50 \mu\text{m}$ to be smaller than the ion penetration depth, $60\text{--}70 \mu\text{m}$. The same samples were studied by magneto-optical imaging. The strong Meissner screening and large uniform enhancement of pinning have shown that the irradiation had produced uniformly distributed defects (Prozorov et al., 2010b).

Indeed, to see the effect, we need to start with the best (largest exponent) sample we have. We irradiated the sample designated as batch #2 with $n = 2.83$, which was discussed in detail earlier (see Figs. 18.8, 18.9, and 18.15). To analyze the power-law behavior and its variation with irradiation, we plot $\Delta\lambda$ as a function of $(t = \frac{T}{T_c})^{n_0}$ in Fig. 18.20, where the n_0 values for FeCo122 and FeNi122 were chosen from the best power-law fits of the unirradiated samples (see Fig. 18.21). While the data for unirradiated samples appear as almost perfect straight lines showing robust power-law behavior, the curves for irradiated samples show downturns at low temperatures indicating smaller exponents. This observation, emphasized by the plots of the derivatives $\frac{d\Delta\lambda(t)}{dt^{n_0}}$ in the inset of Fig. 18.20, points to a significant change in the low-energy excitations with radiation.

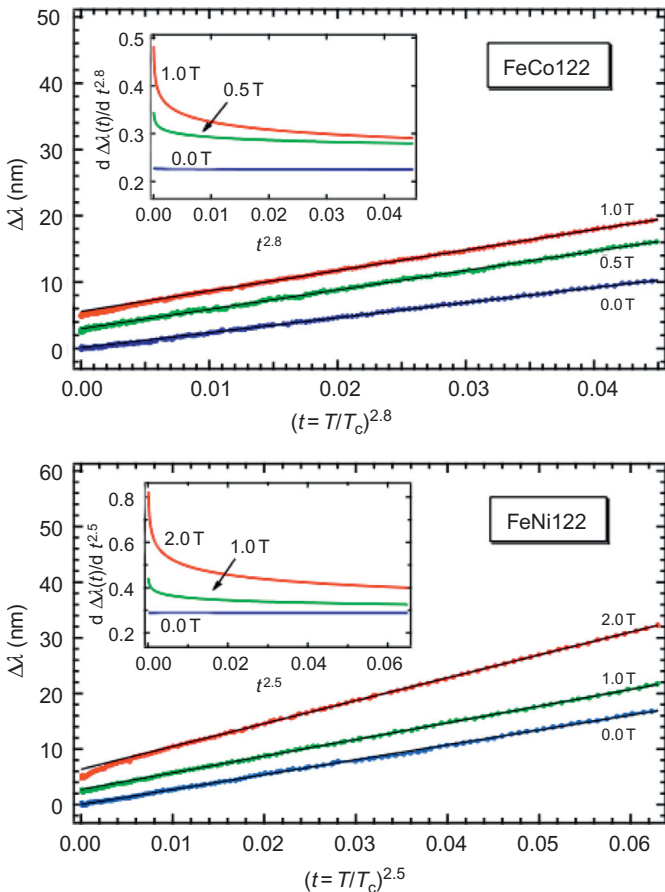


Figure 18.20 Detailed comparison of the functional form of $\Delta\lambda(T)$ for irradiated FeCo122 and FeNi122. In the main panels, $\Delta\lambda(T)$ is plotted versus $(t = T/T_c)^{n_0}$ with the exponents n taken from the best fits of unirradiated samples: $n_0 = 2.8$ and 2.5 for FeCo122 and FeNi122, respectively. Apparently, irradiation causes low-temperature deviations, which are better seen in the derivatives, $d\Delta\lambda(t)/dt^{n_0}$, plotted in the insets.

The variations of T_c and n upon irradiation are illustrated in Fig. 18.21. Dashed lines and circles show FeCo122, while solid lines and triangles designate FeNi122. The upper panel shows the variation of T_c and the width of the transition. Since B_ϕ is directly proportional to the area density of the ions, d , we can say that T_c decreases roughly linearly with d . The same trend is evident for the exponent n shown in the lower panel of Fig. 18.21.

The influence of impurities, assuming s_\pm pairing, has been analyzed numerically in a T -matrix approximation (Kim et al., 2010). Figure 18.22a shows calculated superfluid densities for different values of the scattering rate. Figure 18.22b shows corresponding densities of states. Finally, Fig. 18.22c shows the central result: the

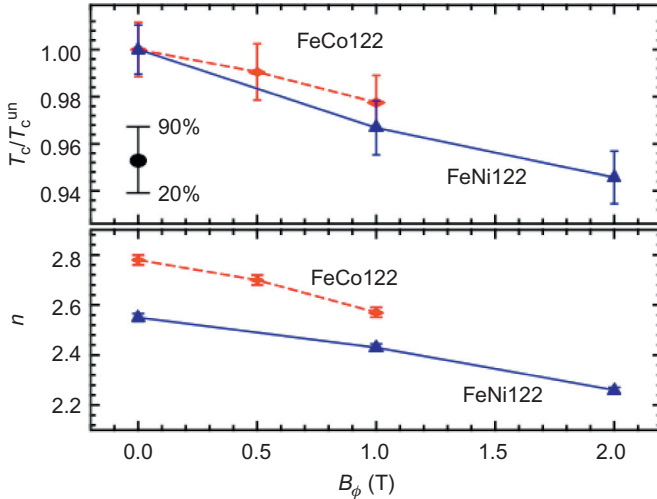


Figure 18.21 Top panel: The suppression of T_c with disorder relative to *unirradiated* T_c^{un} . The vertical bars denote the width of the transition corresponding the diamagnetic signal change from 90% (onset) to 20% (end). Symbols are shown at the mean values between onset and end of the transition. Lower panel: Exponent n versus B_ϕ .

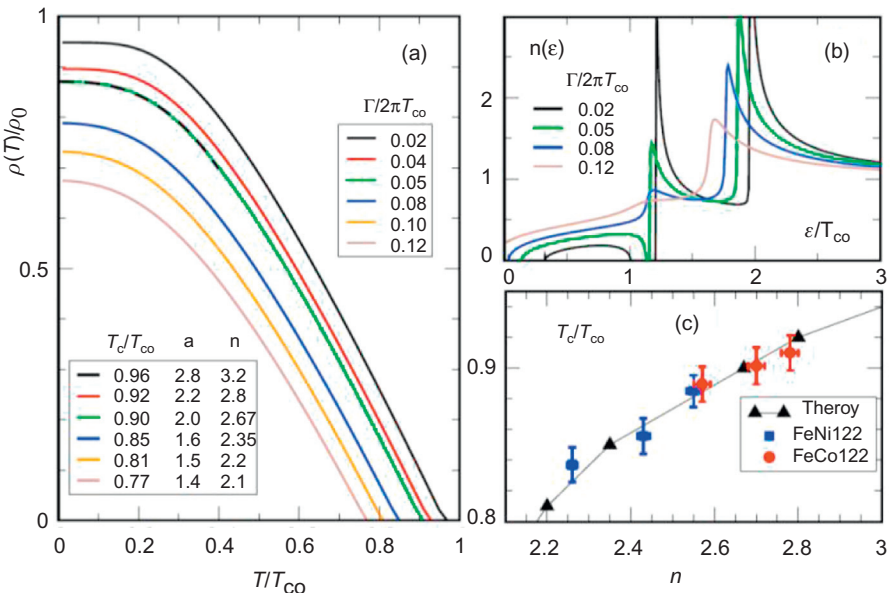


Figure 18.22 (a) Superfluid density and (b) the density of states, computed for the s_{\pm} state with sign-changing isotropic gaps and strong interband impurity scattering, between the Born and unitary limits. The dashed line in (a) is an example of a power-law fit $\rho(T)/\rho_0 = \rho(0)/(1 - a(T/T_{\text{co}})^n)$ for $0 < T < 0.4 T_{\text{co}}$; (b) As the impurity concentration ($n_{\text{imp}} \sim \Gamma$) increases, the band of mid-gap states approaches the Fermi level and the exponent n is reduced. (c) T_c versus power n , from the theoretical model (triangles) and experiment (squares and circles).

correlation between T_c and n . Note that these two quantities are obtained independently of each other. Assuming that the unirradiated samples have some disorder due to doping, and scaling T_c^{un} to lie on the theoretical curve, we find that the $T_c(B_\phi)$ of the irradiated samples also follows this curve. The assumption of a similarity between doping and radiation-induced disorder, implied in this comparison, while not unreasonable, deserves further scrutiny. More recent discussion on the variation of T_c with disorder is found in Efremov et al. (2011).

Conclusion

It was not possible to include in this chapter many interesting results obtained for various members of the diverse family of iron-based superconductors. However, we may provide some general conclusions based on our work as well as on results reported by others.

1. The superconducting gap in optimally doped pnictides is isotropic and nodeless.
2. Pair-breaking scattering changes the clean-limit low-temperature asymptotics (exponential for nodeless and T -linear for line nodes) to a $\sim T^2$ behavior. Therefore, additional measurements (such as deliberately introduced disorder) are needed to reach reliable conclusions about the order parameter symmetry. In anisotropic superconductors in general and in s_{\pm} , in particular, even the nonmagnetic impurities are pair-breaking.
3. These materials can be described within a self-consistent two-band γ -model with two gaps and the ratio of the magnitudes of about $\frac{\Delta_1(0)}{\Delta_2(0)} \approx 2 - 3$.
4. Upon doping, the power-law exponent, n , for the in-plane penetration depth, $\lambda_{ab}(T)$, decreases, reaching values below 2, signaling the developing of significant anisotropy, whereas out-of-plane $\lambda_c(T)$ shows a linear- T behavior indicating line nodes with the Fermi velocity predominantly in the c -direction.
5. There is a fairly large region of coexisting superconductivity and long-range magnetic order, albeit with a suppressed superfluid density.
6. Overall, the observed behavior is consistent with the s_{\pm} pairing, but more realistic 3D calculations are required to achieve agreement with experiment.

References

- Abrikosov, A.A. Fundamentals of the Theory of Metals. North Holland, 1988a. Copyright 2001 ACS CAPLUS AN 1995:736940 CAN 123:150356 56-12 Nonferrous Metals and Alloys 76, 76 Japan. Written in Japanese. Electronic structure; Superconductivity (fundamentals of theory of superconductive metals); Alloys; Metals Role: PRP (Properties) (fundamentals of theory of superconductive metals).
- Abrikosov, A.A., Gor'kov, L.P., 1960. Zh. Eksp. T. Fiz. 39, 1781 (Sov. Phys. JETP 12, 1243 (1961)).
- Bang, Y., 2009. Europhys. Lett. 86 (4), 47001.
- Bean, C.P., 1964. Rev. Mod. Phys. 36 (1), 31–39.
- Bobowski, J.S., Baglo, J.C., Day, James, Dosanjh, P., Ofer, Rinat, Ramshaw, B.J., et al., 2010. Phys. Rev. B. 82 (9), 094520.

- Bouquet, F., Wang, Y., Fisher, R.A., Hinks, D.G., Jorgensen, J.D., Junod, A., et al., 2001. *Europhys. Lett.* 56 (6), 856.
- Brinkman, A., Golubov, A.A., Rogalla, H., Dolgov, O.V., Kortus, J., Kong, Y., et al., 2002. *Phys. Rev. B.* 65 (18), 180517.
- Canfield, P.C., Bud'ko, S.L., 2010. *Ann. Rev. Cond. Matt. Phys.* 1 (1), 27.
- Ding, H., Richard, P., Nakayama, K., Sugawara, K., Arakane, T., Sekiba, Y., et al., 2008. *Europhys. Lett.* 83, 47001.
- Dolgov, O.V., Kremer, R.K., Kortus, J., Golubov, A.A., Shulga, S.V., 2005. *Phys. Rev. B.* 72 (2), 024504.
- Dolgov, O.V., Golubov, A.A., Parker, D., 2009. *New J. Phys.* 11 (7), 075012.
- Efremov, D.V., Korshunov, M.M., Dolgov, O.V., Golubov, A.A., Hirschfeld, P.J., 2011. *Phys. Rev. B.* 180512.
- Eilenberger, G., 1968. *Zeitschrift für Physik A Hadrons and Nuclei.* 214, 195. Available from: <http://dx.doi.org/doi:10.1007/BF01379803>.
- Evtushinsky, D.V., Inosov, D.S., Zabolotnyy, V.B., Koitzsch, A., Knupfer, M., Büchner, B., et al., 2009. *Phys. Rev. B.* 79, 054517.
- Fernandes, R.M., Pratt, D.K., Tian, W., Zarestky, J., Kreyssig, A., Nandi, S., et al., 2010. *Phys. Rev. B.* 81, 140501.
- Fletcher, J.D., Carrington, A., Taylor, O.J., Kazakov, S.M., Karpinski, J., 2005. *Phys. Rev. Lett.* 95, 097005.
- Fletcher, J.D., Carrington, A., Diener, P., Rodiere, P., Brison, J.P., Prozorov, R., et al., 2007. *Phys. Rev. Lett.* 98, 057003.
- Gasparov, V.A., Sidorov, N.S., Zver'kova, I.I., 2006. *Phys. Rev. B.* 73 (9), 094510.
- Gofryk, K., Sefat, A.S., Bauer, E.D., McGuire, M.A., Sales, B.C., Mandrus, D., et al., 2010. *New J. Phys.* 12 (2), 023006.
- Golubov, A.A., Mazin, I.I., 1997. *Phys. Rev. B.* 55 (22), 15146.
- Gordon, R.T., Vannette, M.D., Martin, C., Nakajima, Y., Tamegai, T., Prozorov, R., 2008. *Phys. Rev. B.* 78, 024514.
- Gordon, R.T., Martin, C., Kim, H., Ni, N., Tanatar, M.A., Schmalian, J., et al., 2009a. *Phys. Rev. B.* 79, 100506.
- Gordon, R.T., Ni, N., Martin, C., Tanatar, M.A., Vannette, M.D., Kim, H., et al., 2009b. *Phys. Rev. Lett.* 102, 127004.
- Gordon, R.T., Kim, H., Salovich, N., Giannetta, R.W., Fernandes, R.M., Kogan, V.G., et al., 2010. *Phys. Rev. B.* 82, 054507.
- Graser, S., Kemper, A.F., Maier, T.A., Cheng, H.-P., Hirschfeld, P.J., Scalapino, D.J., 2010. *Phys. Rev. B.* 81, 214503.
- Hardy, F., Wolf, T., Fisher, R.A., Eder, R., Schweiss, P., Adelmann, P., et al., 2010. *Phys. Rev. B.* 81 (6), 060501.
- Hardy, W.N., Bonn, D.A., Morgan, D.C., Liang, R., Zhang, K., 1993. *Phys. Rev. Lett.* 70 (25), 3999.
- Hashimoto, K., Shibauchi, T., Kasahara, S., Ikada, K., Tonegawa, S., Kato, T., et al., 2009a. *Phys. Rev. Lett.* 102 (20), 207001.
- Hashimoto, K., Shibauchi, T., Kato, T., Ikada, K., Okazaki, R., Shishido, H., et al., 2009b. *Phys. Rev. Lett.* 102 (1), 017002.
- Hashimoto, K., Yamashita, M., Kasahara, S., Senshu, Y., Nakata, N., Tonegawa, S., et al., 2010. *Phys. Rev. B.* 81 (22), 220501.
- Hauser, J.J., 1972. *J. Low Temp. Phys.* 7, 335.
- Hirschfeld, P.J., Goldenfeld, N., 1993. *Phys. Rev. B.* 48, 4219.
- Hosono, H., 2008. *J. Phys. Soc. Jap.* 77SC (Suppl. C), 1.

- Jiang, S., Xing, H., Xuan, G., Wang, C., Ren, Z., Feng, C., et al., 2009. *J. Phys.: Condens. Matter.* 21, 382203.
- Johnston, D.C., 2010. *Adv. Phys.* 59 (6), 803.
- Kamihara, Y., Watanabe, T., Hirano, M., Hosono, H., 2008. *J. Am. Chem. Soc.* 130 (11), 3296.
- Kamihara, Y.Y., Hiramatsu, H., Hirano, M., Kawamura, R., Yanagi, H., Kamiya, T., et al., 2006. *J. Am. Chem. Soc.* 128 (31), 10012.
- Kim, H., Gordon, R.T., Tanatar, M.A., Hua, J., Welp, U., Kwok, W.K., et al., 2010. *Phys. Rev. B.* 82 (6), 060518.
- Kim, H., Tanatar, M.A., Song, Y.J., Kwon, Y.S., Prozorov, R., 2011a. *Phys. Rev. B.* 83 (10), 100502.
- Kim, H., Tanatar, M.A., Shen, Bing, Hai-Hu Wen, Prozorov, R., 2011b. arXiv:1105.2265.
- Klein, T., Braithwaite, D., Demuer, A., Knafo, W., Lapertot, G., Marcenat, C., et al., 2010. *Phys. Rev. B.* 82 (18), 184506.
- Kogan, V.G., 2002. Macroscopic anisotropy in superconductors with anisotropic gaps. *Phys. Rev. B.* 66 (2), 020509.
- Kogan, V.G., 2009. *Phys. Rev. B.* 80 (21), 214532.
- Kogan, V.G., Martin, C., Prozorov, R., 2009. *Phys. Rev. B.* 80 (1), 014507.
- Liu, C., Takeshi Kondo, A.D., Palczewski, G.D., Samolyuk, Y., Lee, M.E., Tillman, Ni. Ni., et al., 2009. *Physica C.* 469 (9–12), 491.
- Luan, L., Auslaender, O.M., Lippman, T.M., Hicks, C.W., Kalisky, B., Chu, J.H., et al., 2010. *Phys. Rev. B.* 81 (10), 100501.
- Luan, L., Lippman, T.M., Hicks, C.W., Bert, J.A., Auslaender, O.M., Chu, J.H., et al., 2011. *Phys. Rev. Lett.* 106 (6), 067001.
- Luetkens, H., Klauss, H.-H., Khasanov, R., Amato, A., Klingeler, R., Hellmann, I., et al., 2008. *Phys. Rev. Lett.* 101 (9), 097009.
- Luo, X.G., Tanatar, M.A., Reid, J.P.h., Shakeripour, H., Doiron-Leyraud, N., Ni, N., et al., 2009. *Phys. Rev. B.* 80, 140503.
- Maiti, S., Korshunov, M.M., Maier, T.A., Hirschfeld, P.J., Chubukov, A.V., 2011. arXiv:1104.1814.
- Malone, L., Fletcher, J.D., Serafin, A., Carrington, A., Zhigadlo, N.D., Bukowski, Z., et al., 2009. *Phys. Rev. B.* 79, 140501.
- Markowitz, D., Kadanoff, L.P., 1963. *Phys. Rev.* 131 (2), 563.
- Martin, C., Tillman, M.E., Kim, H., Tanatar, M.A., Kim, S.K., Kreyssig, A., et al., 2009a. *Phys. Rev. Lett.* 102, 247002.
- Martin, C., Gordon, R.T., Tanatar, M.A., Kim, H., Ni, N., Bud'ko, S.L., et al., 2009b. *Phys. Rev. B.* 80, 020501.
- Martin, C., Kim, H., Gordon, R.T., Ni, N., Thaler, A., Kogan, V.G., et al., 2010a. *Sci. Tech.* 23 (6), 065022.
- Martin, C., Kim, H., Gordon, R.T., Ni, N., Kogan, V.G., Bud'ko, S.L., et al., 2010b. *Phys. Rev. B.* 81, 060505.
- Mazin, I.I., 2010. *Nature.* 464 (7286), 183.
- Mazin, I.I., Singh, D.J., Johannes, M.D., Du, M.H., 2008. *Phys. Rev. Lett.* 101 (5), 057003.
- Mishra, V., Boyd, G., Graser, S., Maier, T., Hirschfeld, P.J., Scalapino, D.J., 2009. *Phys. Rev. B.* 79 (9), 094512.
- Mishra, V., Graser, S., Hirschfeld, P.J., 2011. arXiv:1101.5699.
- Mizuguchi, Y., Takano, Y., 2010. *J. Phys. Soc. Jap.* 79 (10), 102001.
- Nakajima, M., Ishida, S., Kihou, K., Tomioka, Y., Ito, T., Yoshida, Y., et al., 2010. *Phys. Rev. B.* 81, 104528.

- Nandi, S., Kim, M.G., Kreyssig, A., Fernandes, R.M., Pratt, D.K., Thaler, A.N., et al., 2010. Phys. Rev. Lett. 104, 057006.
- Nefyodov, Y.A., Shubaev, A.M., Trunin, M.R., 2005. Europhys. Lett. 72 (4), 638.
- Ni, N., Bud'ko, S.L., Kreyssig, A., Nandi, S., Rustan, G.E., Goldman, A.I., et al., 2008a. Phys. Rev. B. 78, 014507.
- Ni, N., Tillman, M.E., Yan, J.-Q., Kracher, A., Hannahs, S.T., Bud'ko, S.L., et al., 2008b. Phys. Rev. B. 78, 214515.
- Ni, N., Thaler, A., Yan, J.Q., Kracher, A., Colombier, E., Bud'ko, S.L., et al., 2010a. Phys. Rev. B. 82, 024519.
- Ni, N., Thaler, A., Kracher, A., Yan, J.Q., Bud'ko, S.L., Canfield, P.C., 2010b. Phys. Rev. B. 80, 024511.
- Nicol, E.J., Carbotte, J.P., 2005. Phys. Rev. B. 71 (5), 054501.
- Okazaki, R., Konczykowski, M., van der Beek, C.J., Kato, T., Hashimoto, K., Shimozawa, M., et al., 2009. Phys. Rev. B. 79 (6), 064520.
- Padamsee, H., Neighbor, J.E., Shiffman, C.A., 1973. J. Low Temp. Phys. 12, 387. Available from: <http://dx.doi.org/doi:10.1007/BF00654872>.
- Paglione, J., Greene, R., 2010. Nat. Phys. 6, 645.
- Pokrovskii V.L., 1961. 40, 641 (Zh. Eksp. Teor. Fiz. V.L. Pokrovskii, Thermodynamics of anisotropic superconductors, Sov. Phys. JETP 13, 447 (1961)).
- Prozorov, R., Giannetta, R.W., 2006. Supercon. Sci. Tech. 19 (8), R01.
- Prozorov, R., Giannetta, R.W., Carrington, A., Fournier, P., Greene, R.L., Guptasarma, P., et al., 2000a. Appl. Phys. Lett. 77 (25), 4202.
- Prozorov, R., Giannetta, R.W., Carrington, A., Araujo-Moreira, F.M., 2000b. Phys. Rev. B. 62 (1), 115.
- Prozorov, R., Tanatar, M.A., Gordon, R.T., Martin, C., Kim, H., Kogan, V.G., et al., 2009a. Physica C. 469, 582.
- Prozorov, R., Tanatar, M.A., Blomberg, E.C., Prommapan, P., Gordon, R.T., Ni, N., et al., 2009b. Physica C. 469, 667.
- Prozorov, R., Gurevich, A., Luke, G., 2010a. Supercon. Sci. Tech. 23 (5), (special issue).
- Prozorov, R., Tanatar, M.A., Roy, B., Ni, N., Bud'ko, S.L., Canfield, P.C., et al., 2010b. Phys. Rev. B. 81 (9), 094509.
- Reid, J.-P., Tanatar, M.A., Luo, X.G., Shakeripour, H., Doiron-Leyraud, N., Ni, N., et al., 2010. Phys. Rev. B. 82 (6), 064501.
- Reid, J.-P., Tanatar, M.A., Luo, X.G., Shakeripour, H., de Cotret, S.R., Doiron-Leyraud, N., et al., 2011. arXiv:1105.2232.
- Ren, Z., Tao, Q., Jiang, S., Feng, C., Wang, C., Dai, J., et al., 2009. Phys. Rev. Lett. 102 (13), 137002.
- Ren, Z.-A., Lu, W., Yang, J., Yi, W., Shen, X.L., Li, Z.C., et al., 2008. Chin. Phys. Lett. 25, 2215.
- Rotter, M., Tegel, M., J., Dirk, 2008. Phys. Rev. Lett. 101 (10), 107006.
- Sefat, A.S., Jin, R., McGuire, M.A., Sales, B.C., Singh, D.J., Mandrus, D., 2008. Phys. Rev. Lett. 101 (11), 117004.
- Senga, Y., Kontani, H., 2008. J. Phys. Soc. Jpn. 77 (11), 113710.
- Shibauchi, T., Hashimoto, K., Okazaki, R., Matsuda, Y., 2009. Physica C. 469 (9–12), 590.
- Song, Y.J., Ghim, J.S., Yoon, J.H., Lee, K.J., Jung, M.H., Ji, H.S., et al., 2011. Europhys. Lett. 94, 57008.
- Sonier, J.E., Huang, W., Kaiser, C.V., Cochrane, C., Pacradouni, V., Sabok-Sayr, S.A., et al., 2011. Phys. Rev. Lett. 106, 127002.
- Stewart, G.R., 2011. arXiv:1106.1618.

- Takahash, H., Imai, Y., Komiya, S., Tsukada, I., Maeda, A., 2011. arXiV:1106.1485.
- Tanatar, M.A., Ni, N., Samolyuk, G.D., Bud'ko, S.L., Canfield, P.C., Prozorov, R., 2009a. Phys. Rev. B. 79 (13), 134528.
- Tanatar, M.A., Ni, N., Martin, C., Gordon, R.T., Kim, H., Kogan, V.G., et al., 2009b. Phys. Rev. B. 79, 094507.
- Tanatar, M.A., Reid, J.P.h., Shakeripour, H., Luo, X.G., Doiron-Leyraud, N., Ni, N., et al., 2010. Phys. Rev. Lett. 104 (6), 067002.
- Thomale, R., Platt, C., Hanke, W., Hu, J., Andrei Bernevig, B., 2011. arXiV:1101.3593.
- Valdés Aguilar, R., Bilbro, L.S., Lee, S., Bark, C.W., Jiang, J., Weiss, J.D., et al., 2010. Phys. Rev. B. 82 (18), 180514.
- Van Degrift, C.T., 1975. Rev. Sci. Instrum. 46 (5), 599.
- Vorontsov, A.B., Vavilov, M.G., Chubukov, A.V., 2009. Phys. Rev. B. 79 (14), 140507.
- Wei, F., Chen, F., Sasimal, K., Lv, B., Tang, Z.J., Xue, Y.Y., et al., 2010. Phys. Rev. B. 81 (13), 134527.
- Williams, T.J., Aczel, A.A., Baggio-Saitovitch, E., Bud'ko, S.L., Canfield, P.C., Carlo, J.P., et al., 2009. Phys. Rev. B. 80 (9), 094501.
- Williams, T.J., Aczel, A.A., Baggio-Saitovitch, E., Bud'ko, S.L., Canfield, P.C., Carlo, J.P., et al., 2010. Phys. Rev. B. 82 (9), 094512.
- Wilson, J.A., 2010. J. Phys.: Cond. Mat. 22 (20), 203201.
- Wu, D., Barišić, N., Dressel, M., Cao, G.H., Xu, Z.A., Carbotte, J.P., et al., 2010. Phys. Rev. B. 82 (18), 184527.
- Xu, Y.-M., Huang, Y.-B., Cui, X.-Y., Razzoli, E., Radovic, M., Shi, M., et al., 2011. Nat. Phys. (advance online publication).
- Yong, J., Lee, S., Jiang, J., Bark, C.W., Weiss, J.D., Hellstrom, E.E., et al., 2011. arXiV:1101.5363.